Accepted Manuscript

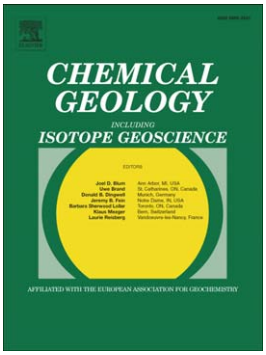

Insights into mantle-type volatiles contribution from dissolved gases in artesian waters of the Great Artesian Basin, Australia

F. Italiano, G. Yuce, I.T. Uysal, M. Gasparon, G. Morelli

PII: S0009-2541(14)00200-9
DOI: doi: 10.1016/j.chemgeo.2014.04.013
Reference: CHEMGE 17207

To appear in: *Chemical Geology*

Received date: 8 August 2013
Revised date: 15 April 2014
Accepted date: 17 April 2014

Please cite this article as: Italiano, F., Yuce, G., Uysal, I.T., Gasparon, M., Morelli, G., Insights into mantle-type volatiles contribution from dissolved gases in artesian waters of the Great Artesian Basin, Australia, *Chemical Geology* (2014), doi: 10.1016/j.chemgeo.2014.04.013

Insights into mantle-type volatiles contribution from dissolved gases in artesian waters of the Great Artesian Basin, Australia

F. Italiano[*], *G. Yuce, I.T. Uysal, M. Gasparon, G. Morelli*

*** Corresponding author: Dr F. Italiano f.italiano@pa.ingv.it**

Tel. +390916809411

Insights into mantle-type volatiles contribution from dissolved gases in artesian waters of the Great Artesian Basin, Australia

F. Italiano[1], G. Yuce[2,3,4], I.T. Uysal[2], M. Gasparon[2,5,6], G. Morelli[5]*

1 – Istituto Nazionale di Geofisica e Vulcanologia, sezione di Palermo, Italy

2 - The Queensland Geothermal Energy Centre of Excellence, The University of Queensland, QLD, Australia

3 - Eskisehir Osmangazi University, Department of Geological Engineering, Meselik, Turkey

4-Hacettepe University, Department of Geological Engineering, Beytepe, Ankara, Turkey

5 – School of Earth Sciences, The University of Queensland, QLD, Australia

6 – Australian National Centre for Groundwater Research and Training

Abstract

The geochemical features of the volatiles dissolved in artesian thermal waters discharged over three basins (Millungera, Galilee and Cooper basin) of the Australian Great Artesian Basin (GAB) consistently indicate the presence of fluids from multiple gas sources located in the crust (e.g. sediments, oil reservoirs, granites) as well as minor but detectable contributions of mantle/magma-derived fluids. The gases extracted from 19 water samples and analyzed for their chemical and isotopic composition exhibit amounts of CO_2 up to about 340 mlSTP/L_{H2O} marked by a $\delta^{13}C_{TDC}$ (Total Dissolved Carbon) ranging from -16.9 to +0.18‰ vs PDB, while CH_4 concentrations vary from $4.4x10^{-5}$ to 4.9 mlSTP/L_{H2O}. Helium contents were between 9 and >2800 times higher than equilibrium with Air Saturated Water (ASW), with a maximum value of 0.12 mlSTP/L_{H2O}. Helium isotopic composition was in the 0.02-0.21Ra range (Ra = air-normalized $^3He/^4He$ ratio). The three investigated basins differ from each other in terms of both chemical composition and isotopic signatures of the dissolved gases whose origin is attributed to both mantle and crustal volatiles. Mantle He is present in the west-central and hottest part of the GAB despite no evidence of recent volcanism. We found that the partial pressure of helium, significantly higher in crustal fluids than in mantle-type volatiles, enhances the crustal He signature in the dissolved gases, thus masking the

original mantle contribution. Neotectonic activity involving deep lithospheric structures and magma intrusions, highlighted by recent geophysical investigations, are considered to be the drivers of mantle/magmatic volatiles towards the surface. The results, although pertaining to artesian waters from a vast area of >542,000 km^2, provide new constraints on volatile injection, and show that fluids' geochemistry can provide additional and independent information on the geo-tectonic settings of the Great Artesian Basin and its geothermal potential.

1 - Introduction

The Great Artesian Basin (GAB) of Australia is unique not only because it is the largest and deepest artesian basin in the world, but also because it experiences conspicuously elevated crustal and mantle degassing in association with high heat production (Habermehl and Pestov, 2002; Torgersen et al., 1992). Highly radioactive crust in the central-western part of the GAB is responsible for an increase in heat flow and regional ^{4}He flux, whereas the reduced heat flow with enhanced ^{3}He flux is attributed to young volcanism in its eastern part (Sass and Lachenbruch, 1978; Torgersen et al., 1987; Duncan and McDougall, 1989; Torgersen et al., 1992). Eastern Australia has been the site of both hotspot volcanism and intraplate lava flow fields since the late Cretaceous (Wellman and McDougal, 1974). Hotspot volcanism occurs as a response to the northward migration of Australia away from Antarctica, and is currently centered in Bass Strait in southeast Australia. Intraplate lava flow fields are distributed across the east coast in time and space, but the most recent activity (< 5 Ma) is concentrated in northeast Queensland and southern Victoria (Johnson, 1989; Vasconcelos et al., 2008). A ^{3}He-rich gas component indicating a mantle contribution of up to 7% in the GAB groundwater was observed at localities (at ~20.5 S° 144° E, ~25.5 S° 146° E, and ~27 S° 144.5° E) in close proximity to Cenozoic lava flow fields (Torgersen et al., 1987; Torgersen et al., 1992), however to date there has been no evidence suggesting a mantle helium input to the groundwater further west, in the central and hottest part of the GAB. Natural gases from the Eromanga and Cooper Basins underlying the central-western part of the GAB, however, have extremely high CO_2

contents of more than 50%, although gases from most Australian basins contain CO_2 of <5% (Boreham et al., 2001). Gases with CO_2 contents >5% in association with narrowly ranging $\delta^{13}C$ values between -3 and -10‰ in the Eromanga and Cooper Basins are considered to be originated from a mantle source (Boreham et al., 2001). Although no surface manifestation of volcanic activity is present in this region, it has been demonstrated elsewhere that mantle volatiles can be transferred into the shallow crust following extensional tectonic activity (Oxburgh and O'Nions, 1987; Kennedy and van Soest, 2006; Banerjee et al., 2011). The injection of mantle-derived fluids into geothermal reservoirs and groundwaters can be detected using the He isotope geochemistry of volatiles even in regions where there is no active volcanism (e.g., Italiano et al., 2000; Gulec et al., 2004; Kulongoski et at. 2005; Italiano et al., 2013). The aims of this article are to evaluate the chemical and isotopic composition of the whole gas phase dissolved in deep artesian waters to explore whether a mantle fluid flux occurs in the central part of the GAB, and to discuss implications for active tectonics, and heat source and geothermal potential in the central GAB. A broad scale survey was conducted to collect gases dissolved in artesian thermal waters throughout the Galilee and Millungera Basins, and the northern part of the Cooper Basin in SW Queensland (Figure 1). Water samples were taken from 19 deep artesian wells mostly in areas that have not been sampled by previous investigators (Torgersen et al, 1987; Torgersen et al., 1992), and analyzed for dissolved gas contents (He, CO_2, CH_4, N_2 and O_2), and He, Ar and C isotopes.

2 - Geological Background and Hydrology

The GAB comprises the Mesozoic Eromanga, Surat and Carpentaria Basins and parts of the Permian Bowen and Galilee Basins (Habermehl, 2001a, b, and references therein). The confined aquifers occur in quartzose sandstones of continental origin and mostly Triassic, Jurassic and Cretaceous ages. The most productive aquifers in the GAB are the Lower Cretaceous-Jurassic sequences, with about 500 - 1500 mg/L total dissolved solids and bore yields over 5 L/sec. A thick Early Cretaceous argillaceous sequence of marine origin is the main confining unit. The

groundwater recharge zone is located primarily along the eastern margin of the basin, and the large-scale regional groundwater flow direction is from the east towards the southwest.

The geology of the GAB consists of several broad synclinal structures trending north and northeast, overlying sedimentary, metamorphic and igneous rocks of pre-Jurassic or pre-Triassic ages. The Mesozoic sedimentary sequence in the central part of the basin reaches a maximum total thickness of about 3000 m (Habermehl, 2001). Parts of the marginal areas of the basin have been eroded, in particular along the eastern border, which was uplifted during Cainozoic times. Several major fault and fold systems occur in the basin, in places forming en-echelon structures. The Eromanga Basin sequence was deformed during the mid-Tertiary by relatively mild northeast-southwest compression (Langford et al, 1995). Faulting reactivation caused a significant displacement in the Eromanga Basin sequence, locally reaching 780 m (Radke et al., 2000) during the last 95 Ma (Jones and Veevers, 1983; Wellman, 1987). Evidence for neotectonic activity in the GAB has been reported for the Lake Eyre region in northern South Australia, where Miocene-age sediments are clearly deformed. These include deformed bedding planes, small-scale folds, faults and fracture systems reflecting consistent Miocene and younger tectonic activity in central Australia (Waclawik et al., 2008).

The densely faulted basement of the Galilee basin is overlaid with the Upper Carboniferous-Lower Permian Joe Joe Group, which is composed of quartzose sandstone and minor conglomerate with argillaceous beds. The uppermost unit of the Galilee Basin contains conglomerate, micaceous lithic sandstone and micaceous siltstone (Triassic Moolayember Formation). The basin overlies a crystalline basement that is step-faulted with downthrows to the west. The NE-trend is constrained by the Warrego Fault, with the Pleasant Creek Arch (a fault-bend anticline) as its southern boundary. Folding occurred during the deposition in the Galilee Basin. The Lovelle Depression, a shallower through, is located along the northwestern margin of the Galilee Basin. The Canaway Fault, the main normal fault in the GAB, separates the Galilee from the Cooper and the Warbuton Basins, which extend from south-east Queensland into north-west South Australia.

The Cooper Basin comprises a ~2 km-thick sequence of late Carboniferous and Permian glacial deposits (Merimellia and Tirrawarra Formations), deformed along NE-SW tectonic ridges (Gidgealpa-Merrimelia-Yanapurra ridges) and separated by paleo-depressions (Patchawarra, Nappamerri, Allunga and Tenappera troughs; PIRSA 2010). It hosts major geothermal, oil and gas deposits (Chopra, 2003; Wyborn et al. 2004). The Cooper Basin is overlaid by the 3 km-thick Mesozoic sequence of the Eromanga Basin.

The Millungera Basin, which is completely covered by a thin succession of sediments of the Jurassic–Cretaceous Eromanga-Carpentaria Basin, has been recently discovered based on the interpretation of aeromagnetic data and deep seismic reflection surveys (Korsch et al., 2011).

There are about 4700 flowing artesian and 20,000 non-flowing artesian water wells in the GAB, with further 3500 petroleum exploration and production wells. The depth of the water wells ranges from a few hundred metres to almost 4 kilometres.

3 - Sampling and analytical procedures

In order to gain insight into the gas phases released over the GAB, we sampled 19 thermal waters (outlet temperatures ranging between 35 and 87 °C) from free-flowing artesian wells in November-December 2011 (Table 1), since no venting or bubbling gases are known to occur over the studied basins (Galilee, Millungera and Cooper). Some of the artesian waters have already been considered for their helium (Torgersen et al., 1992) and carbon (Boreham et al., 2001) isotopic systematics, but the composition of the dissolved gases has been obtained for the first time in this study. Our samples, collected specifically for the extraction of the whole gas phase for chemical and isotopic analyses, were stored in 240 ml pyrex bottles sealed in the field using rubber/teflon septa and purpose-built pliers, and analyzed within one month. Details of the sampling methodology are reported in Italiano et al. (2009, 2013) and further information on its suitability for both chemical and helium isotopic analysis is reported in the Appendix. The depth of the sampled bores ranged from 183 to 3903 metres (Table 1). Only wells with the screen close to the base of the bore were

sampled, to ensure that the water sampled at the surface was representative of the deep groundwater, and therefore that mixing with the shallower fluids would be minimized.

In the laboratory, the dissolved gases were extracted after equilibrium was reached at constant temperature with a host-gas (high-purity argon) injected in the sample bottle (for further details see Italiano et al., 2009, 2013). Chemical analyses were carried out by gas-chromatography (Perkin Elmer Clarus500 equipped with a double TCD-FID detector) using argon as the carrier gas. Typical uncertainties were within ± 5%.

Helium isotope analyses were carried out on gas fractions extracted following the same procedure or, alternatively, on the already exsolved gas phase, and purified following methods described in the literature (Hilton 1996; Sano and Wakita, 1988; Italiano et al 2001). The isotopic analyses of the purified helium were performed using a static vacuum mass spectrometer (GVI5400TFT) that allows the simultaneous detection of ^{3}He and ^{4}He ion beams, thereby keeping the $^{3}He/^{4}He$ error of measurement to very low values. Typical uncertainties in the range of low-^{3}He samples are within ± 2%.

The isotopic composition of carbon from total dissolved carbon ($\delta^{13}C_{TDC}$) was measured on 2ml of water sample introduced in containers where high purity helium was injected to remove atmospheric CO_2. The water samples were acidified with phosphorus pentoxide in an auto-sampler to ensure complete release of CO_2 from acidified waters. CO_2 was then directly admitted to a continuous flow mass spectrometer (AP2003). The extracted CO_2 amounts represent the total content of dissolved carbon (TDC). The results are reported in δ‰ units relative to the V-PDB (Vienna –Pee Dee Belemnite) international standard. Standard deviation of the $^{13}C/^{12}C$ ratio was ± 0.2 ‰.

Argon isotopes were measured by a multi-collector noble gas mass spectrometer (ARGUS, GVI) specifically designed for simultaneous measurement of ^{40}Ar, ^{38}Ar and ^{36}Ar isotopes using a detector that holds five Faraday collectors. ^{40}Ar is detected on a collector with a 10^{11} ohm resistor, and the remaining isotopes are collected and measured on four detectors fitted with 10^{12} ohm resistors (for

^{36}Ar to ^{39}Ar). The equipment is connected to a stainless steel purification line where 0.1ml of gas is introduced and purified by cold and hot getter pumps (reactive gas removal). Measuring errors are estimated to be smaller than ± 1%.

4 - Results

Table 1 lists the sample locations together with the depth of the wells and the T (°C), pH, electrical conductivity (EC, in μS/cm), and oxidation-reduction potential (ORP, in mV) field data. Data for dissolved gas compositions, expressed in $mlSTP_s/L_{H2O}$, are presented in Table 2. Helium and C isotopic compositions and $^{4}He/^{20}Ne$ ratios are reported in Table 3, while the available Ar isotope data (samples 11-15, 17 and 19) are listed in Table 4.

Starting from the gas-chromatographic analyses, the composition of the dissolved gas phase was calculated by combining the solubility coefficients (Bunsen coefficient "β", ml_{gas}/L_{H2O}) of each gas species at the equilibration temperature, the volume of gas extracted (ml), and the volume of the water sample as shown in equation (1):

$$G_C = \{[G_{gc}] * V\gamma_e + ([G_{gc}] * \beta_G * VW)\} VW^{-1} * V\gamma_e * V\gamma_i^{-1}/100 \quad (1)$$

where G_C is the concentration of the selected gas specie, G_{gc} is its concentration measured by gas chromatography (vol%), $V\gamma_e$ and $V\gamma_i$ represent the extracted and the introduced gas volumes, respectively, while *VW* is the volume of the analyzed water sample (see also Italiano et al., 2009 and 2013 for further details). All volumes are carefully measured at the equilibration temperature.

The analytical results of Table 2 show the presence of variable oxygen amounts in all vented thermal fluids. The N_2/O_2 ratios, often used to detect the presence of an atmospheric component, are well above (up to about 100 times) the N_2/O_2 ratio in Air Saturated Water (ASW) (4.8mlSTP/L) in the majority of the artesian waters, except for a few samples (column 8, Table 2) that have N_2/O_2 values close to the atmospheric ratio (~2). The most abundant non-atmospheric component is CO_2, whose content is well above the equilibrium with ASW (0.24 $mlSTP/L_{H2O}$; Weiss, 1974) in the three basins, ranging from about 10 times (average for Millungera), to 50-200 times (for Galilee)

and up to 1400 times the equilibrium value at Bonnie Doon (Cooper Basin). CH_4 is always present with concentrations ranging from $4.4x10^{-5}$ mlSTP/L_{H2O} at Julia Creek Railway well, and 4.9 mlSTP/L_{H2O} at Longreach. The isotopic composition of the Total Dissolved Carbon ($\delta^{13}C$ TDC) ranges between -16.91 and +0.18, with different average values over the three basins (Table 3).

Samples from the Millungera Basin display negligible CH_4 content (average $5x10^{-2}$ mlSTP/L_{H2O}) but are enriched in He. In contrast, volatiles from the Galilee and Cooper Basins have higher CH_4 contents (up to two orders of magnitude, on average 1.5 and 1.2 mlSTP/L_{H2O}, respectively), and differ from each other in their helium content (higher in the Cooper relative to the Galilee Basin).

Helium concentrations, well above the equilibrium with ASW ($4.8x10^{-5}$mlSTP/L_{H2O}), vary from about $6x10^{-4}$ to $1.2x10^{-1}$mlSTP/L_{H2O} with an isotopic signature ranging from $0.01Ra_c$ to $0.1Ra_c$ (where c stands for "corrected values").

5 - Discussion

5.1 – Dissolved gas phase assemblage

A mixture of volatiles of different origin than the atmosphere is recognized to be a common feature at the investigated basins (Table 2). The non-atmospheric gas species, CO_2, CH_4 and He may either originate from crustal-derived products including granites, metasediments and oil reservoirs, or from mantle-derived products intruded in the crust or releasing mantle volatiles through lithospheric discontinuities.

The atmospheric contribution in terms of N_2/O_2 values (Table 2) is significantly different among the three basins, which can be roughly classified as air-depleted (Cooper), air-enriched (Galilee), and intermediate (Millungera). The two samples from Innot Hot Springs falling within the overlapping fields of the Millungera and Galilee Basins represent a separate group and are different from each other in their O_2 and CO_2 content.

Considering the low (and often negative) ORP values (Table 1) besides a N_2 content well above the equilibrium with ASW, the dissolved O_2 appears to be mainly due to local infiltration of shallow

waters (e.g. from the periodical flooding affecting the Australian outback) and/or the consequence of contamination (due to well construction and possibly leakage) of the deep artesian groundwaters by shallow air-equilibrated waters.

The O_2-He-CO_2 triangular diagram (Figure 2) shows the relationships between gas species typically representative of the atmosphere (O_2) and other sources (namely crust and mantle). Gas/water interaction (GWI) processes (arrows in Figure 2) seem to be responsible for the composition of the dissolved gas assemblage: deep-originated volatiles (containing CO_2 and He) rise towards the surface, and interact with air-equilibrated groundwaters (ASW, represented by O_2 in Figure 2). Further GWI accounts for CO_2 dissolution.

Apart from the obvious CO_2 enrichment in volcanic areas, the venting of CO_2-rich waters has been observed in geothermal areas well-known for their CO_2-rich thermal springs (e.g Yellowstone, Wairakei or Larderello geothermal systems), in tectonically active continental areas (e.g. North and East Anatolian Fault Zone, Turkey Italiano et al., 2013) where CO_2-rich thermal waters bring a mixture of mantle-derived and metamorphic CO_2, and in the seismically active Central Apennines (Italy) where CO_2-rich springs carry gaseous CO_2 produced by mechano-chemical reactions (Italiano et al., 2008). The CO_2 extracted from our thermal waters may have been supplied by either a crustal or a mantle source. In order to further constrain the origin of the dissolved volatiles, their carbon isotopic composition was investigated and considered together with information from the light noble gases (He, Ne, Ar) .

5.2 Carbon-He-Ar systematics

5.2.1- Carbon

CO_2 is a very reactive gas with very high solubility in water. Its isotopic composition can be easily modified by a large spectrum of geochemical processes. When involved in gas/water interaction, gaseous CO_2 equilibrates isotopically with HCO_3^- and CO_3^{2-} ions in the aqueous phase, and the mole fraction of each species is a function of the pH of the solution. The $\delta^{13}C_{TDC}$ values reported in

Table 3 represent the average of the isotopic composition of the dissolved carbon species, expressed as the isotopic balance of dissolved carbon species weighted on the respective carbon contents as:

$$\delta^{13}C_{TDIC} = (\delta^{13}C_{CO2\,aq} * \chi CO_{2aq} + \delta^{13}C_{HCO3} * \chi HCO_3)/M \quad (2)$$

where χ is the molar fraction and M is the total mass of dissolved carbon. CO_2(aq) and HCO_3^- are the predominant carbon species at the pH range (6.1-8.7, Table 1) of the sampled waters, therefore the observed $\delta^{13}C$ values for dissolved inorganic carbon ($\delta^{13}C_{TDIC}$) are a function of the mole fraction of HCO_3^-.

Since GWI processes that resulted in carbon fractionation may have occurred at variable extent during gas uprising and CO_2 dissolution, we recalculated the theoretical isotopic composition of the gaseous CO_2 interacting with the groundwaters. According to Deines et al., (1974) and Zhang et al., (1995) the $\delta^{13}C_{CO2aq}$ and $\delta^{13}C_{HCO3}$ can be computed considering the isotope enrichment factors (ε) for the CO_{2gas} - HCO_3 (ε_α) and the CO_{2gas} - CO_{2aq} (ε_β) systems. The isotopic ratio of the gaseous CO_2 can be recalculated as

$$\delta^{13}C_{CO2} = \delta^{13}C_{TDIC} - [\varepsilon_\alpha * \chi HCO_3 + \varepsilon_\beta \chi CO_2] \quad (3)$$

The results, reported in Table 3, show how the pristine gaseous CO_2 had an isotopic signature more negative by some 2-5 ‰ with respect to the TDC, except for the sample from Bonnie Doon.

The $\delta^{13}C_{CO2}$ vs CO_2 content (mlSTP/L_{H2O}) plotted in Figure 3 (*a*) shows two main groups, one of which includes samples from the Millungera and Galilee Basins with $\delta^{13}C_{CO2}$ values ranging from -22.72 to -10.02‰, and the other, including samples from the Cooper Basin, from -9.06 to -0.59‰. For both groups the more negative is the $\delta^{13}C$, the lower is the CO_2 content, thus representing variable extents of GWI processes. Apart from the GWI, the observed $\delta^{13}C$ ranges are consistent with the presence of different CO_2 reservoirs feeding the ground waters that circulate over the studied basins, in agreement with previous studies (Boreham et al., 2001).

The natural CO_2 sources are marked by different $\delta^{13}C$ ratios ($\delta^{13}C_{MORB}$ = - 6.5‰; $\delta^{13}C_{Limestones}$ = 0‰, $\delta^{13}C_{Marine\ sediments}$ = -20‰; Faure, 1977; Javoy et al., 1986; Sano and Marty, 1995), although

mixing of volatiles from different sources and fractionation processes may produce similar $\delta^{13}C$ values. The range of measured carbon isotopic compositions for TDC ($-16.91‰ < \delta^{13}C_{TDC} < +0.18‰$) and CO_2 ($-21.08‰ < \delta^{13}C_{CO2} < -1.37‰$) allows us to exclude a main input of organic CO_2 (typically ranging from -70‰ to -25‰) to the deep gas phase. The isotopically heavy carbon ($\delta^{13}C_{TDC}$+0.18‰, $\delta^{13}C_{CO2}$ -1.37) of Nockatunga (Cooper Basin) suggests a contribution from carbonate devolatilization, likely sourced from high-temperature water-rock interactions or from over-mature sediments (Sun, 1997). Although any high-temperature interaction requires a thermal source (e.g. the mantle, Italiano et al., 2008), CO_2 from this site is isotopically different from those of the Cooper Basin (as well as those of the Gippsland and Bonaparte basins; Boreham et al., 2001), which are normally depleted in heavy carbon ($\delta^{13}C<-10$ ‰), despite the extremely high CO_2 contents. Variable degrees of degassing may account for the loss of the light (^{12}C) carbon isotope from the pristine CO_2-dominated gas phase released at Nockatunga. Since Boreham et al. (2001) pointed out that gases with CO_2 contents >5% and falling in the range $-3<\delta^{13}C<-10‰$ are considered to be derived from an inorganic igneous and/or mantle source (Smith and Pallasser, 1996), we argue that although CO_2-rich volatiles from multiple sources may feed the same basin, there is a clear contribution from the mantle either directly (volatiles degassing) or indirectly (conductive thermal energy).

Figure 3*b* shows the CO_2 content against the CH_4 content. The samples fall along a broadly increasing trend for the two gas species, showing that despite the occurrence of GWI, the two gas species are closely linked together. Considering that 1) CH_4 is not a major component in mantle fluids, 2) CH_4 may be released from hydrocarbon reservoirs, but in this case it would not be linearly correlated with CO_2 as shown in Figure 3b; 3) CH_4 is abundant in geothermal reservoirs where, in the presence of water, the reactive carbon species (CH_4, CO and CO_2) equilibrate as a function of the local P-T conditions (e.g. Italiano and Nuccio, 1991; Italiano et al., 2013), we propose that geothermal systems where volatiles equilibrate during their rise towards the surface can be

responsible for CH_4 production and for the observed CO_2-CH_4 relationships. In line with this proposition, the isotopic composition of the bubbling gas from the hottest sample (Birdsville, Cooper Basin; $\delta^{13}C_{CH4}$ =-45‰ and δD_{CH4}= -175‰) indicates a thermogenic origin for CH_4 (Schoell M., 1980, 1988), and thus supports the existence of high-temperature geothermal reservoirs.

5.2.2 –Helium

The $^4He/^{20}Ne$ ratios (Table 3) denote a low or negligible atmospheric contribution in the sampled waters, in agreement with the chemical composition of the dissolved gases, assuming that all ^{20}Ne is of atmospheric origin.

The isotopic composition of the dissolved helium (Table 3) has been corrected for atmospheric contamination using the air-normalized $^4He/^{20}Ne$ ratio multiplied by the ratio of its Bunsen coefficient (see caption of Figure 4). The air-corrected $^3He/^4He$ ratios (R/Ra_c) of the dissolved helium range between 0.01 and $0.1Ra_c$ (Table 3). Most of the measured helium isotopic ratios fall within the range of crustal helium (0.02-0.05Ra; Table 3), although the corrected ratios at Winton ($0.08Ra_c$), Longreach ($0.09Ra_c$) and Quilpie ($0.09Ra_c$), all in the Galilee Basin, are higher than typical crustal values. Additional ^3He inputs to the local ground waters may thus only be due to mantle-derived volatiles permeating at depth. It is noteworthy that the highest and the lowest $^3He/^4He$ values were recorded within the Millungera Basin: at Nelie ($0.1Ra_c$) and Kynuna (0.01Rac). The latter is consistent with the $^3He/^4He$ ratio expected from in situ radiogenic production in crustal lithologies (Andrews, 1985; Mamyrin and Tolstikhin, 1984; Ballentine and Burnard, 2002), while the former denotes contributions from a ^3He-rich source. We argue that it would be very unlikely for ^3He-rich volatiles (either from the mantle or from magmatic intrusions) to move towards the surface across the granites located at depth (Korsch et al., 2001) in the absence of active tectonic structures. Reactivation of truncated thrust faults that occur along the western and eastern margin of the Millungera Basin (Car et al., 2010) may have facilitated the migration of ^3He-rich volatiles to the surface. Recent geophysical studies show local low seismic velocity anomalies in the

Millungera Basin (Saygin et al., 2013), which may be associated with fault-controlled local occurrences of mantle-derived and/or heated fluids. Indeed, the highest $^{3}He/^{4}He$ value ($0.1Ra_c$) at Nelie coincides with a low seismic velocity and gravity anomaly (location 6 in Saygin et al., 2013).

MORB-like volatiles in the Australian lithospheric mantle have been revealed by the geochemical composition of the noble gases trapped in CO_2-rich fluid inclusions from southeastern Australia (Matsumoto et al, 1998, 2000; 2009), which is marked by a mean $^{3}He/^{4}He$ ratio of $1.1\pm0.2x10^{-5}$, and within the range reported for MORBs ($1.2\pm0.1x10^{-5}$; ~8 Ra; Hilton et al., 1993; Farley and Neroda, 1998; Ozima and Igarashi, 2000). Mantle-type volatiles are incorporated in ground waters at Mt Gambier (up to 3Ra; Chivas et al., 1987) and in the eastern GAB (0.81 Ra; Love et al., 2009) and western GAB (0.16Ra at Warburton Spring, and 0.72Ra at Bubbler Spring; Love et al., 2009). The $^{3}He/^{4}He$ ratios of our samples fall in the 0.01-$0.1Ra_c$ range, indicating ^{3}He injections accompanied by significant amounts of dissolved CO_2. To evaluate the extent of mantle volatile contribution to the dissolved gas phase as well as elemental fractionations between He and CO_2, we examined the correlation between $CO_2/^{3}He$ and CO_2 (Figure 4a) and between $CO_2/^{3}He$ and R/Ra_c (Figure 4b).

$CO_2/^{3}He$ ratios plotted against dissolved CO_2 content describe an apparent trend (Figure 4a) up to a maximum $CO_2/^{3}He$ value of $5.9x10^{11}$ as the CO_2 contents increase. This $CO_2/^{3}He$ value was recorded at Bonnie Doon (Cooper Basin), and the crustal $^{3}He/^{4}He$ ratio of 0.02Ra reflects also a possible addition of ^{3}He-depleted, CO_2–dominated volatiles potentially derived from hydrothermal devolatilization of carbonates (see $\delta^{13}C$ values in Table 3 and Figure 3). In the plot of $CO_2/^{3}He$ versus R/Ra_c (Figure 4b), the absence of any correlation suggests that the observed $CO_2/^{3}He$ ratios are not the result of simple mixing between crustal and mantle volatiles. In Figure 4b, the crustal volatiles should plot within the area defined by R/Ra_c of up to 0.05 and $CO_2/^{3}He$ ratios up to 10^{14}, however the highest ratio is lower than 10^{12}. Almost all the samples from the Galilee Basin plus two from the Cooper and one from the Millungera Basin show small but measurable additions of ^{3}He-rich volatiles. GWI processes are responsible for the CO_2 loss that largely changes the $CO_2/^{3}He$ ratios, moving the samples along the trends (dotted line) shown in Figure 4a.

The amount of helium that dissolves in the deep ground waters following GWI is a function of the molar fraction of helium in the gas phase. Since the helium molar fraction in mantle-type volatiles (in the range of 0.9-20x10^{-4}vol%; e.g., Fisher et al. (1998), and references therein) is 2-4 orders of magnitude lower than in crustal fluids (3000-5000x10^{-4} vol%; e.g., Fourrè et al. (2011)), it can be expected that the dissolved crustal-derived helium be dominant when the basal flux is made of volatiles from both crustal and mantle sources.

The $^{4}He/^{20}Ne$ vs R/Ra_c graph in Figure 5 shows that almost all the samples fall between the mixing lines of atmosphere with upper and lower continental crust, here assumed to be carbonate-enriched (upper crust) and made of granitic and crystalline rocks (lower crust). Some helium isotope values, however, are not compatible with such a simple atmosphere-crust (either upper or lower) mixing model, suggesting contributions from a ^{3}He-enriched source. We constructed two theoretical curves that broadly fit those values (mainly from the Galilee Basin) by adding to the upper crust, (taken as 0.05Ra) 25% and 50% contributions of Mt Gambier-type helium (3Ra; Love et al., 2009). The aim of Figure 5 is not to quantify the percentage of mantle contribution to the dissolved gases, but to highlight the presence of fluids that can be considered as "intermediate" fluids carrying 2–15% mantle He (Pik and Marty, 2008) over the three investigated basins.

The data published in Torgersen et al. (1992) provide further support to the model presented here. Some of the Ra values measured in central Australia (black filled circles in Figure 5) are similar to the values measured in this study (e.g., in Birdsville) or are even higher (0.59Ra in Oakwood and 0.568Ra in Juanbang). The ^{3}He-^{4}He-CO_2 ternary diagram in Figure 6 provides further support to our findings. The sample distribution on the graph shows variable extents of CO_2 dissolution, as well as the addition of ^{3}He. As the ^{3}He content is calculated from the helium isotopic ratios corrected for atmospheric contamination (albeit very low or insignificant; see Table 3), the ^{3}He addition can only have a mantle origin.

5.2.3 - Argon

Due to its high solubility in water, the presence of argon in any ASW is mainly due to atmospheric contribution, thus is normally not very useful to measure Ar isotopic ratios in dissolved gases. Some samples, however, displayed free gas separated from the water inside the sealed sampling bottle, therefore they were selected for spectrometric analyses of ^{36}Ar, ^{40}Ar, and ^{4}He concentration together with their $^{40}Ar/^{36}Ar$ isotopic composition. Helium and Ar concentrations range from 76 to >2000x10^{-4} vol%, and from 1211 to >12000x10^{-4} vol%, respectively (Table 4). These values are well above the air content (5.2 and 9780x10^{-4} vol%, respectively; Table 4) and do not represent variable extents of air contamination. The ^{40}Ar concentrations corrected for atmospheric contribution range from 14 to 139 ppm, suggesting a measurable argon contribution from endogenic sources, in agreement with the corrected $^{40}Ar/^{36}Ar$ isotopic ratios of up to 306.3 (Table 4). The data in Figure 7 (*a, b*) show two trends of crustal and mantle volatiles contributions in terms of argon versus helium isotopes, consistent with the results of the chemical and isotopic compositions of CO_2 and He.

5.3 - Mantle fluid injection and the role of neotectonics

The presented geochemical features of the dissolved gases indicate multiple volatile sources including spatially variable proportions of deeply-derived (endogenic) fluids. The presence of significant amounts of CO_2, CH_4 and He with $^{3}He/^{4}He$ values higher than the typical range for crustal fluids of 0.02-0.05Ra indicate that deep mantle-derived fluids can rise to the surface through the ductile lower crust and brittle upper crust. Considering the general assumption that fluid passage through the impermeable ductile lower crust is difficult (e.g. Kennedy and van Soest, 2007), the fundamental question to be dealt with is how mantle volatiles are injected into the crustal-fluid system in a continental intraplate tectonic setting.

The passage of mantle fluids through the ductile boundary can occur by mantle decompression beneath thin continental crust leading to partial melting and degassing of mantle-derived magmas (Ballentine et al., 2002b). In regions void of active or recently active volcanism, as is the case in

the study area, a magmatic flow of mantle fluids through the ductile lower crust can also occur due to the creation of permeable pathways as a result of crustal deformation (Kulongoski et al., 2005; Kennedy and van Soest, 2007). Crustal deformation and the associated seismic activity in continental intraplate regions occur commonly through reactivation of pre-existing zones of weakness such as regions of extended continental crust (c.f., Johnston and Kanter, 1990; Kato et al., 2009).

Australia is the most rapidly moving continent globally, drifting north at a current speed of approximately 7 cm/year (Kennett and Blewett, 2012). The northward movement resulted in collision with Eurasia in the Timor and Papua New Guinea regions (Huston et al., 2012), with the plate boundary forces acting upon the Australian Plate and inducing a compressional stress regime in central and eastern Australia (Hillis and Muller, 2003). The Australian continent is thus one of the most seismically active intraplate regions in the world. A number of major recent reverse fault earthquakes involving surface fault rupture have occurred in central Australia, with many pre-historic fault scarps having been discovered (McCue, 1990). The main regions of documented neo-tectonic activity in Australia are the extended crustal areas, particularly those representing Mesozoic major rifting episodes, where normal faults have been reactivated as reverse faults under compression (Clark et al., 2011). The most prominent examples of neotectonic activity are found in South Australia in the Flinders and Mount Lofty Ranges, which are bound to the East and the West by reverse faults that thrust Proterozoic and/or Cambrian basement rocks above Quaternary sediment (Quigley et al., 2006). A number of faults have been documented in this region showing Pliocene to Quaternary displacements (see Clark et al., 2011 and references therein). Further north and closer to the study area in Queensland (Lake Eyre region), the deformation of Miocene-age sediments is the obvious consequence of neotectonic activity (Waclawik et al., 2008). A number of historical earthquakes with magnitudes between 3 and 7 have been recorded in central Australia, particularly in northern South Australia, southwest Queensland and the Northern Territory (Hillis et al., 2008; see also http://www.quakes.uq.edu.au). Samples with R/Ra values indicating

contributions of mantle volatiles seem to be located along significant fault systems and may indicate litospheric faults. In contrast, samples (e.g # 11, 12, and 13) with low R/Ra values (crustal-type volatiles), although occuring in intensely faulted areas, may indicate the presence of shallow faults (Fig. 1).

Another indicator of neotectonic activity in the southwestern GAB is the widespread occurrence of springs and sinter deposits, which occur along faults extending from the basement to the surface (Adlam and Kuang, 1988). Some recent pilot studies have confirmed the role of neotectonics in the creation of pathways that allow the migration of deeply-sourced CO_2-rich fluids in the groundwater system (Uysal et al., 2013). Travertine deposits in southwest Queensland and northern South Australia are particularly significant, as they form due to CO_2 degassing when the highly carbonated groundwaters emerge along faults. Some of the carbonate and silica sinter deposits in the southwestern GAB are intensely fractured and show evidence of faulting. Field observations and structural mapping near Lake Eyre showed that pre-existing faults were reactivated neotectonically and controlled the formation of late Quaternary carbonate vein and breccia deposits, which formed in hydro-fractures during the release of overpressured CO_2-rich fluids (Uysal et al., 2013). High precision U-series dating of carbonate veins suggests that the release of the pressurised CO_2 occurred intermittently from 35.9 ± 0.15 ka to 1.2 ± 0.02 ka (Uysal, unpublished data), possibly in association with mantle degassing in response to seismicity, analogous to similar deposits in seismically active geothermal systems worldwide (Hancock et al., 1999; Rihs et al., 2000; Chiodini et al., 2004; Newell et al., 2005; Uysal et al., 2007; Uysal et al., 2009).

5.4 Heat origin and potential for geothermal resources in the GAB

The release of mantle-derived volatiles implies a large amount of CO_2 as well as the supply of significant amounts of thermal energy to fluids located in crustal levels, including ground waters and oil reservoirs. The release of conductive thermal energy by granites at shallow crustal levels (upper crust) differs from the typically convective thermal energy of mantle origin released at the

level of the lower crust (or deeper). Therefore, the new conceptual model for the GAB needs to incorporate individual sub-basins with varying chemistry, flow paths and mixing dynamics and temperature conditions.

Seismic tomography techniques have been used extensively lo locate geothermal anomalies (e.g., Foley et al., 1992; Munoz et al., 2010; Muksin et al., 2013). Low seismic velocity anomalies in central Australia recorded by Saygin and Kennett (2010) coincide with areas where high heat flow anomalies occur (Chopra and Holgate, 2005). These regions are also defined by the thinnest crust in the Australian continent, approximately 30 km thick, in the southern extension of the study area in southwest Queensland and northeast South Australia (Kennett et al., 2011). Substantially higher heat flows (113.0±2.9 mW/m^2 and 107.5±1.7 mW/m^2) have been reported further north in the Millungera Basin. These values are well above the regional average of 65–90 mW/ m^2 (Faulkner et al. 2012; Fitzell et al. 2012), and correspond to low seismic velocity regions (Saygin et al., 20133; see also section 5.2.2) possibly caused by higher heat production due to deep crustal fracturing and/or neotectonic fault reactivation, and hence mantle heat release at a scale smaller than the whole GAB.

6 - Conclusions

Analysis of dissolved gases in artesian waters of the GAB revealed the presence of CO_2 (up to about 340 cm^3 CO_2 mlSTP/L_{H2O}) and significant amounts of helium (up to $1.2x10^{-1}$ mlSTP/L_{H2O}). $\delta^{13}C_{CO2}$ and $^3He/^4He$ as high as -1.37‰ and 0.1 Rac, respectively, suggest the presence of a deep mantle-derived source for some of the released He and CO_2. A mantle contribution ranging from 0.5% to 2.5% is estimated based on the $^3He/^4He$ isotope systematics of the GAB waters investigated in this and previous studies, with the largest component inferred for the Galilee Basin.

Recent seismic tomography studies are consistent with our gas geochemistry results, suggesting that deep crustal fracturing and degassing, and hence heat released from the mantle, occur at a scale smaller than the whole GAB.

Volatiles from different sources (both shallow and deep) contribute to feed the circulating waters that move across tectonic structures and discontinuities, generating a wide array of geochemical signatures. The geochemical features of dissolved He and CO_2 are consistent with the proposed presence of mantle-derived CO_2 over the Cooper basin (Boreham et al., 2001) and the area's anomalously high heat flow (Sass and Lachenbruch, 1978; Cull and Conley, 1983; Torgersen et al., 1992; Beardsmore, 2004; Chopra and Holgate, 2005; Korsch et al., 2011). The gas geochemistry data contribute to better constrain the groundwater flow path by highlighting the geochemical variability of the vented fluids over the three investigated basins, and provide further evidence that the GAB cannot be considered as a single and relatively simple water reservoir. More detailed small-scale studies including structural mapping are needed to conclusively establish the link between faulting and mantle degassing.

Acknowledgements

This work was financially supported by the Queensland Geothermal Energy Centre of Excellence, the National Institution for Geophysics and Volcanology-INGV (Italy), the Eskisehir Osmangazi University (Turkey) (project no. 2011/15022), and the Australian National Centre for Groundwater Research and Training. Two anonymous reviewers and the editor in chief David Hilton whose comments and suggestions greatly improved the final version of the paper are kindly acknowledged. The authors wish to thank Hugh Russell and Glenda Heyde for their valuable help to carry out this project. The authors are indebted to Hal Gurgenci and Andrew Glikson for their valuable comments and suggestions. Mauro Martelli, Andrea Rizzo, Marcello Liotta and Fausto Grassa are kindly acknowledged for their support during the laboratory work.

Appendix

Helium permeation through pyrex glass

Helium diffusion through pyrex glass is known to be a potentially serious problem for sample storage before helium isotope analysis due to the rate of helium diffusion through pyrex glass bottles (e.g. Sano and Fisher, 2012). For this reason, pyrex bottles are not commonly used for the collection of fluids/gases for helium isotope analysis. However, as optimization of sampling and analytical methods must be based on scientific evidence, all available experimental information must be considered before a certain procedure can be adopted or deemed to be unsuitable for a specific purpose. In this appendix, we review the available evidence for He diffusivity through pyrex glass, and argue that pyrex glass bottles are suitable for the sampling and storage of fluids/gases for He isotope analysis as long as the storage time does not exceed two months.

In a recent paper by Sano and Fisher (2012), the problem of long-time storage of samples for helium isotopic analysis is discussed considering the permeation constant of pyrex glass of 1.5×10^{-11} ccSTP/sec/cm^2/mm/Torr (at 25°C), experimentally determined by Norton (1953). Sano and Fisher (2012) calculated a permeation rate of 3.2×10^{-6} ccSTP/day of total helium for a pyrex bottle with 280 cm^2 inner surface area, 0.7 mm thick glass, 300 ml internal volume, an internal helium concentration of 1.3 vol% and atmospheric helium concentration outside the bottle ($\Delta P \approx 10$Torr = 7.5×10^{-2}Pa). Under these conditions, it would take 10 years for the sample to equilibrate with the atmosphere. This is a short time compared to lead glass, whose permeation constant is lower by one order of magnitude (9.1×10^{-12} ccSTP/sec/cm^2/mm/Torr; Norton, 1953), and thus implying an equilibration time of the order of one century.

Figure A1 shows the permeability rates as a function of the He partial pressure gradient for different surface areas and thicknesses. Considering a helium concentration inside the pyrex bottle of 100 ppm (10^{-2}%), the permeability rate ranges from 1.5×10^{-6} to 3×10^{-4} ccSTP/day. The range is 1×10^{-5} to 2×10^{-3} ccSTP/day for a 1% He concentration. At this rate, a gas sample stored in our 240 ml pyrex bottles (inner surface area of 367 cm^2 and 3mm wall thickness) will take about 10 years to equilibrate with the atmospheric helium concentration, almost irrespective of the initial He concentration within the range 100 ppm to 1% (Figure A2).

Since the permeability rates are direct and linear functions of surface area, , time and concentration gradient, and inverse function of thickness, a decrease in helium concentration by an order of magnitude leads to an equilibration time of one millennium for leaded glass. Therefore, a storage time of up to 2-3 years in leaded glass will not compromise the sample's integrity (Sano and Fisher, 2012).

The case of water samples for dissolved gas analyses.

Water samples collected for dissolved gas analyses typically require further laboratory procedures for gas extraction. The sampling bottles are not filled with gas, and therefore the pyrex glass surface area through which helium can permeate is not the whole inner surface area of the bottle, but only that of the gas bubble formed by gas exsolution and/or water volume contraction due to cooling. For example, for a 240 ml water sample collected at 85 °C, a temperature drop of 60 °C to room temperature (assumed to be 25 °C) generates a volume contraction of 3.024 ml (estimated considering the volumetric expansion relationship for liquids $\Delta V=KV_0\Delta T$, where K=volumetric thermal expansion coefficient for water = $2.14x10^{-4}$ $°C^{-1}$ and for V_0=240 ml), which creates a bubble that is filled with gases exsolved from the water. Helium can diffuse from this bubble through the glass, but the permeability rate is a function of surface area and thickness of the wall, as well as helium concentration gradient. Under these conditions, the equilibration time between the sample helium and atmospheric helium becomes much longer because of the small exchange surface, although it might also be shorter due to the low amount of helium contained in the gas bubble.

Figure A2 shows three time-dependent trends for the full equilibration of sample helium (inside) with the atmosphere (outside), calculated for gas sample volumes of 3, 10 and 240 ml (representative for bubbles generated by temperature drops of 25 and 60 °C and for a gas-filled bottle, respectively). The horizontal lines highlight the initial sample helium contents of 0.5, 0.03 and 0.002% (ranges recorded in our sample set). The relatively wide concentration range considered

in these calculations also takes into account the helium enrichment in the separated gas phase due to its low solubility in the water phase. It is straightforward to observe that gas in a completely-filled bottle takes a relatively short time to equilibrate with the atmosphere (about 10 years for the considered range of helium contents). In contrast, the gas bubbles need 5 times (or even) longer to equilibrate with the atmosphere due to their reduced exchange surface areas (even considering the maximum spherical section). The conclusion of our calculations is that a long-term storage cannot be considered a reliable procedure for gas samples collected in pyrex bottles; however, it is suitable for water samples as long as the storage time does not exceed a few months.

Samples collected in pyrex bottles for this study were analyzed within two to four weeks from the date of sampling. The first batch was sampled between 5 to 11 November 2011, and the second from 13 to 16 December 2011. All samples were shipped to Italy by fast cargo and were analyzed on 25 November 2011 (first batch) and 9-10 January 2012 (second batch). The maximum He loss within this time frame would be 0.3% (for a large-size bubble with the highest helium content of 0.5% by volume) of the initial content (Figure A3 a, b). For these reasons, we consider the $^{3}He/^{4}He$ values reported in Table 3 as representative of the waters sampled.

Helium isotopes can be fractionated during helium permeation because of the different diffusivity of masses 3 and 4. Following Trull and Kurtz (1999), low isotopic diffusivity ratios ($D^{3}He/D^{4}He$) require significantly large He losses to alter initial $^{3}He/^{4}He$ ratios. Considering a $D^{3}He/D^{4}He=1.15$ (at room temperature - from Graham's Law), the initial $^{3}He/^{4}He$ ratio may be lowered by 10% for a 65% He loss. This value increases to 80% for a diffusivity ratio of 1.08 (Trull and Kurtz, 1999). Considering that the helium loss from our samples is always below 0.5% (even in the worst-case scenario of 0.5% initial He content – see Figure A3b), the resulting isotopic fractionation is negligible and within the measurements error.

Further simulation tests have been carried out to evaluate the temporal changes in isotopic ratio due to the simultaneous ^{4}He-loss/^{3}He-gain through the pyrex walls induced by the different pressure gradients of the two isotopes. Figure A4 shows the simulations for 0.7 and 3 mm pyrex glass wall

thicknesses with internal helium contents of 0.5 and 0.05%. The ^{3}He partial pressure in the dissolved gas sample is calculated from the helium content, the total gas content and the gas/water partition coefficient as a function of temperature. For example, the "Birdsville" sample ($^{3}He/^{4}He$ ratio = 0.06 Ra) has a helium content of $1x10^{-2}$ ccSTP/L and a total gas content of 35.36 ccSTP/L (Table 2). These values yield a ^{3}He partial pressure of $9.86x10^{-8}$ hPa, which is an order of magnitude higher than the atmosphere ($7.28x10^{-9}$hPa). This ^{3}He pressure, always higher than the atmosphere, prevents atmospheric ^{3}He permeation and isotopic fractionation as a function of sample storage time. As a result of the above calculations and considerations, we recommend that samples collected in pyrex glass bottles for dissolved helium analyses must be measured within 3-6 months (depending on their original helium content) from the date of collection.We further note that pyrex glass bottles are not suitable for the long-term storage of water samples because of potential helium leakage through the rubber septum. To avoid atmospheric helium diffusion through the septum, we kept the bottles upside down and with the necks submerged in salty water even during sample shipping and laboratory handling.

The measured helium isotopic ratios in this work, well below the atmospheric value, are consistent with a lack of atmospheric contamination due to ^{3}He permeation through the pyrex or the septum as a consequence of the large ^{3}He partial pressure difference between air and the sample. The results obtained in previous studies using the same sampling equipment and methods (e.g., Italiano et al., 2013 and references therein) show that these precautions make our methodology suitable for the analytical determinations of all dissolved gases (including all the main gases, noble gases and their isotopic composition, and total dissolved carbon isotopes).

To conclude, although no duplicate samples were collected using different containers, we note that the helium isotopic ratio measured in a sample from the Birdsville well (Table A1) collected in copper tubes by Torgersen (1992) and our sample collected twenty years later from the same well but using a pyrex bottle are virtually identical.

References

Adlam, R and Kuang, KS 1988. An investigation of structures controlling discharge of spring waters in the south western Great Artesian Basin. Department of Mines and Energy South Australia, Adelaide.

Ballentine, C. J., Burnard, P. G., 2002. Production, release and transport of noble gases in the continental crust, in: Rev. Mineral. Geochem., edited by Porcelli, D., Ballentine, C. J., Wieler, R., Mineral. Soc. of Am., Washington, D. C. vol. 47, pp. 481–538.

Ballentine, C. J., Burgess, R., and Marty, B. (2002b), Tracing fluid origin, transport and interaction in the crust, vol. 47, edited by D. Porcelli, C. J. Ballentine, and R. Wieler, pp. 539–614, Mineral. Soc. Of Am., Washington, D. C.

Beardsmore, G., 2004. The influence of basement on surface heat flow in the Cooper Basin Exploration Geophysics, 35, 223-235.

Bethke, C. M., Zhao, X., Torgersen, T., 1999. Groundwater flow and the ^{4}He distribution in the Great Artesian Basin of Australia. Jour. Geophys. Res. 104, B6, 12, 999-13,011.

Boreham, C.J., Hope, J.M., Hartung-Kagi, B., 2001. Understanding source, distribution and preservation of Australian natural gas: a geochemical perspective. APPEA Jour. 2001, 523-547.

Cartwright, I., Weaver, T., Tweed, S., Ahearne, D., Cooper, M., Czapnik, K., Tranter, J., 2002. Stable isotope geochemistry of cold CO_2-bearing mineral spring waters, Daylesford, Victoria, Australia: sources of gas and water and links with waning volcanism. Chem. Geol. 185, 71– 91.

Carothers, W.W., Kharaka, Y.K., 1980. Stable isotopes of HCO_3 in oil field waters implications for the origin of CO_2. Geochim. Cosmochim. Acta 44, 323–332.

Cero´n, J.C., Pulido-Bosch, A., Sanz de Galdeano, C., 1998. Isotopic identification of CO_2 from deep origin in thermomineral waters of southeastern Spain. Chem. Geol., 149, 251–258.

Chiodini, G., Cardellini, C., Amato, A., Boschi, E., Caliro, S., Frondini, F. and Ventura, G., 2004. Carbon dioxide Earth degassing and seismogenesis in central and southern Italy. Geophys. Res Lett. 31, L07615.

Chopra, P.N., Holgate, F., 2005. A GIS analysis of temperature in the Australian crust. *Proceedings* World Geothermal Congress 2005. Antalya, Turkey, 24–29 April 2005. 7p.

Clark, D., McPherson, A. and Collins, C.D.N., 2011, Australia's seismogenic neotectonic record: a case for heterogeneous intraplate deformation: Geoscience Australia, Record 2011/11, 95 pp.

Commonwealth of Australia (2010) OzTemp-Interpreted Temperature at 5km depth. Geoscience Australia, https://www.ga.gov.au/products/servlet

Cull, J.P., Conley, D., 1983. Geothermal gradients and heat flow in Australian sedimentary basins. BMR Journal of Australian Geology and Geophysics, 8, p. 329 – 337.

Czuppon, G., Matsumoto, T, Handler, M. R., Matsuda, J.I., 2009. Noble gases in spinel peridotite xenoliths from Mt Quincan, North Queensland, Australia: Undisturbed MORB-type noble gases in the subcontinental lithospheric mantle. Chem. Geol. 266, 19–28.

D'Amore, F., Truesdell, A.H., 1988. A review of equilibrium constants for gaseous species of geothermal interest. Sci. Geol. Bull. 41, 309-332.

Deighton, I., Hill, A.J., 1998. Thermal and burial history. in: Gravestock, D.I., Hibburt, J.E., Drexel, J.F. (Eds.). Petroleum Geology of South Australia. Vol. 4-Cooper Basin. *Department of Primary Industries and Resources, Government of South Australia*, pp. 143–55.

Deines, P., 1970. The carbon and oxygen isotopic composition of carbonates from the Oka Carbonatite complex, Quebec, Canada. Geochim. Cosmochim. Acta 34, 1199– 1225.

Duncan, R.A., McDougall, I., Time-space relationships for Cainozoic intraplate volcanism in eastern Australia, the Tasman Sea and New Zealand. In: J.W. Johnson (Editor),Intraplate Volcanism in Eastern Australia and New Zealand, Cambridge University Press, Cambridge, 43-53, 1989

Epstein, S., Mayeda, T., 1953. Variation of O content of water from natural sources, Geochim. Cosmochim. Acta 4, 213–224.

Faulkners. P., Maxwell, M., O'Connorl, L.K., Sargents. S. N., and Talebi, B., 2012. Coastal Geothermal Energy Initiative GSQ Julia Creek 1: Well completion report and heat flow modelling results. Queensland Geological Record, 2012/05.

Faure, G., 1986. Principles of isotope geology. Wiley New York, 2nd Edition, pp. 589.

Fischer T. P., Giggenbach W. F., Sano Y., Williams S. N., 2008. Fluxes and sources of volatiles discharged from Kudryavy, a subduction zone volcano, Kurile Islands . Earth Planet. Sc. Lett. 160, 81–96.

Fitzell M. J., Maxwell M., O'Connor L. K., Sargent S. N., And Talebi B., 2012. Coastal Geothermal Energy Initiative GSQ Dobbyn 2: Well completion report and heat flow modelling results. Queensland Geological Record, 2012/04.

Foley, J. E., Toksoz, M.N.,and Batini, F., 1992. Inversion of teleseismic travel time residuals for velocity structure in the Larderello Geothermal Field, Italy. Geophysical Research Letters, 19, 5-8.

Fourré E., Di Napoli R., Aiuppa A., Parello F., Gaubi E., Jean-Baptiste P., Allard P., Calabrese S., Ben Mamou A., 2011. Regional variations in the chemical and helium–carbon isotope composition of geothermal fluids across Tunisia. Chem. Geol. 288,, 67–85

Gianelli, G. (1985), On the origin of geothermal CO_2 by metamorphic processes, Boll. Soc. Geol. Ital. 104, 575–584.

Graham, D. W., 2002. Noble gas isotope geochemistry of mid-ocean ridge and ocean island basalts: Characterization of mantle source reservoirs. in: Rev. Mineral. Geochem., edited by Porcelli, D., Ballentine, C. J., Wieler, R., Mineral. Soc. of Am., Washington, D. C. vol. 47, pp. 247–317.

Habermehl, M.A., 2001. Wire-Line Logged Waterbores in the Great Artesian Basin, Australia - Digital Data of Logs and Waterbore Data Acquired by AGSO. Bureau of Rural Sciences

publication, Canberra, Australia, Australian Geological SurveyOrganisation, Australia, Bulletin 245.

Hancock, P.L., Chalmers, R.M.L., Altunel, E. and Cakir, Z., 1999. Travitonics: using travertines in active fault studies. J. Struct. Geol. 21, 8-9, 903-916.

Heeswijck, A.V., 2006. The structure, sedimantology, sequence stratigraphy and tectonics of the northern Drummond and Galilee Basins, central Queensland, Australia. PhD Thesis, Volume: I, James Cook University, Earth and Environmental Sciences, p. 156.

Herczeg, A. L., Torgersen, T., Chivas, A. R., Habermehl, M. A., 1991. Geochemistry of ground waters from the Great Artesian Basin, Australia. J. Hydrol., 126, 225-245.

Hillis, R.R., Sandiford, M., Reynolds, S.D., Quigley, M.C., 2008. Present-day stress, seismicity and Neogene-to-Recent tectonics of Australia's 'passive'margins: intraplate deformation controlled by plate boundary forces. In: Johnson, H., Doré, A.G., Gatliff, R.W., Holdsworth, R., Lundin, E.R., Ritchie, J.D. (Eds.), The Natureand Origin of Compression in Passive Margins. Special Publication, vol. 306. Geological Society, London, pp. 71–90.

Holocher J, Peeters F, Aeschbach-Hertig W, Hofer M, Brennwald M., Kinzelbach W., Kipfer R., (2002) Experimental investigations on the formation of excess air in quasi-saturated porous media. Geochimica et Cosmochimica Acta, 66, 23, 4103–4117

Huston D.L., Blewett, R.S. and Champion, D.C., 2012, The evolution of the Australian continent: Episodes, 35, 23-44.

Italiano, F., Martelli, M., Martinelli, G., Nuccio, P.M., 2000. Geochemical evidences of melt intrusions along lithospheric faults of Irpinian Apennines (Southern Italy): Geodynamic and seismogenetic implications. J. Geophys. Res. 105, B6, 13569-13578.

Italiano, F., Martinelli, G., Nuccio, P. M., 2001. Anomalies of mantle-derived helium during the 1997-1998 seismic swarm of Umbria-Marche, Italy. Geophys. Res. Lett. 28, 5, 839-842.

Italiano, F., Martinelli, G., Plescia, P., 2008. CO_2 degassing over seismic areas: the role of mechanochemical production at the study case of Central Apennines. Pageoph. 165, 1, 75-94.

Italiano, F., Bonfanti, P., Ditta, M., Petrini, R., Slejko, F., 2009. Helium and carbon isotopes in the dissolved gases of Friuli region (NE Italy): geochemical evidence of CO_2 production and degassing over a seismically active area. Chem. Geol. 266, 76–85.

Italiano F., Sasmaz A., Yuce G., Okan O. (2013) Thermal fluids along the East Anatolian Fault Zone (EAFZ): geochemical features and relationships with the tectonic setting. Chemical Geology, 339, 103-114, doi.org/10.1016/j.chemgeo.2012.07.027

Javoy, M., Pineau, F., Delorme, H., 1986. Carbon and nitrogen isotopes in the mantle. Chem. Geol. 57 (1-2), 41-62.

Kato, A., E. Kurashimo, T. Igarashi, S. Sakai, T. Iidaka, M. Shinohara, T. Kanazawa, T. Yamada, N. Hirata, and T. Iwasaki, 2009. Reactivation of ancient rift systems triggers devastating intraplate earthquakes. *Geophys. Res. Lett*., **36**, L05301, doi:10.1029/2008GL036450.

Kendall, C., Coplen ,T.B., 1985. Multisample conversion of water to hydrogen by zinc for stable isotope determination. Anal. Chem., 57, 1437-1440. DOI: 10.1021/ac00284a058

Kennedy, B. M. and van Soest, M.C. 2006. A helium isotope perspective on the Dixie Valley, Nevada, hydrothermal system, Geothermics, 35, 26-43.

Kennett B.L.N., Salmon M., Saygin E. & AusMoho Working Group, 2011. AusMoho: the variation in Moho depth in Australia, Geophys.J.Int., 187, 946-958.

Kennett B.L.N and Blewett R., 2012. Lithospheric framework of Australia, *Episodes*, **35**, 9-22.

Muksin, U., Bauer, K., and Haberland, C., 2013 Seismic Vp and Vp/Vs structure of the geothermal area around Tarutung (North Sumatra, Indonesia) derived from local earthquake tomography. J. Volcanol. Geotherm. Res. 260, 27–42.

Kissin, I.G. and Pakhomov, S.I. (1967), The possibility of carbon dioxide generation at depth at moderately low temperature, Dokl. Akad. Nauk SSSR 174, 451–454.

Korsch, R.J., Struckmeyer, H.I.M., Kirkby, A., Hutton, L.J., Carr, L.K., Hoffmann, K.L., Chopping, R., Roy, I.G., Fitzell, M., Totterdell, J.M., Nicoll, M.G., Talebi, B., 2011. Energy

Potential of the Millungera Basin, a newly discovered basin in North Queensland, APEA Journal, 295-332.

Kulongoski, J.T., Hilton, D.R., Izbicki, J.A., 2005. Source and movement of helium in the eastern Morongo groundwater Basin: the influence of regional tectonics on crustal and mantle helium fluxes. Geochim. Cosmochim. Acta 69, 3857–3872.

Kulongoski, J T., Hilton, D R., Cresswell, R. G., Hostetler, S., Jacobson, G., 2008. Helium-4 characteristics of groundwaters from Central Australia: Comparative chronology with chlorine-36 and carbon-14 dating techniques. J. Hydrol. 348, 176– 194.

Lehmann, B.E., Love, A., Purtschert, R, Collon, P., Loosli, H.H., Kutschera, W., Beyerle, U., Aeschbach-Hertig, W., Kipfer, R., Frape, S.K., Herczeg, A., Moran, J., Tolstikhin, I.N., Groning, M., 2003. A comparison of groundwater dating with ^{81}Kr, ^{36}Cl and ^{4}He in four wells of the Great Artesian Basin, Australia. Earth Planet. Sc. Lett. 211, 237-250.

Love, A., Karlstrom, K., Crossey, L., Rousseau-Gueutin, P., Priestley, S., Shand, P., Fluin, J., 2010. Geochemical and neo-tectonic data provides a new understanding of the hydrogeology of the Great Artesian Basin, International Conference "Transboundary Aquifers: Challenges and New Directions"(ISARM2010), Abstracts book, UNESCO-IHP, p. 40-41.

Love, A., Crossey, L., Karlstrom, K, Hilton, D. R, Wolaver, B. D., Rousseau-Gueutin P., 2009. Toward a new paradigm for the Great Artesian Basin: hydrologic mixing, partitioned sub basins, and mantle influences on groundwater quality. Geological Society of America, Abstracts with Programs. 41, 7, p. 28.

Mamyrin, B. A., Tolstikhin, I. N., 1984. Helium Isotopes in Nature, Elsevier, New York.

Martel D.J., Deak J., Dovenyi P., Horvath F., O'Nions R.K., Oxburgh E.R., Stegena L., Stute M., 1989. Leakage of helium from the Pannonian Basin. Nature, 342, 21-28

Martelli, M., Nuccio, P.M., Stuart, F., Burgess, Ellam R., Italiano, F., 2004. Helium-strontium isotope constraints on mantle evolution beneath the Roman Comagmatic Province, (Italy). Earth Planet. Sc. Lett. 224, 295-308.

McCue, 1990. Australia's large earthquakes and recent fault scarps. Journal of Structural Geology,. 12, 76l-766.

Meixner, T.J., Gunn, P.J., Boucher, R.K., Yeats, A.N., Murray, L., Yeats, T.N., Richardson, L.M., Freares. R.A., 2000. South Australia Exploration Geophysics. 31, 24-32.

Mook, W.G., Bommerson, J.C., Staverman, W.H., 1974. Carbon isotope fractionation between dissolved bicarbonate and gaseous carbon dioxide. Earth Planet. Sci. Lett. 22, 169– 176.

Matsumoto, T., Honda,, M., McDougall, I., O'Reilly, S.Y., Norman, M., Yaxley, G., 2000. Noble gases in pyroxenites and metasomatised peridotites from the Newer Volcanics, southeastern Australia: implications for mantle metasomatism. Chem. Geol. 168, 49–73.

Munoz, G.; Bauer, K.; Moeck, I.; Schulze, A.; Ritter, O., 2010. Exploring the Groß Schönebeck (Germany) geothermal site using a statistical joint interpretation of magnetotelluric and seismic tomography models. *Geothermics*, 39, 1, 35-45.

Newell, D.L., Crossey, L.J., Karlstrom, K.E., Fischer, T.P., Hilton, D.R., 2005. Continental-scale links between the mantle and groundwater systems of the western United States: evidence from travertine springs and regional He isotope data. GSA Today 15, 4–10.

Norton, F. J. (1953), Helium Diffusion Through Glass. Journal of the American Ceramic Society, 36: 90–96. doi: 10.1111/j.1151-2916.

Ozima, M., Podosek, F. A., 2002. Noble Gas Geochemistry. 2nd ed., Cambridge University Press, 286 pp.

Pallasser, R.J., 2000. Recognising biodegradation in gas/oil accumulations through the δ 13C composition of gas components. Org. Geochem, 31, 1,363–73.

Pik, R., Marty, B., 2008. Helium isotopic signature of modern and fossil fluids associated with the Corinth rift fault zone (Greece): Implication for fault connectivity in the lower crust. Chem. Geol. 266, 67–75.

Radke, B., 2009. Hydrocarbon and Geothermal Prospectivity of Sedimentary Basins in Central Australia Warburton, Cooper, Pedirka, Galilee, Simpson and Eromanga Basins. Geoscience Australia Record 2009/25.

Rice, J. R., 1992, Fault stress states, pore pressure distributions, and the weakness of the San Andreas fault, in Evans, B., and Wong, T. F., eds., Earthquake mechanisms and transport properties of rocks: London, Academic Press, p. 475–503.

Rihs, S., Condomines, M. and Poidevin, J.L., 2000. Long-term behavior of continental hydrothermal systems: U-series study of hydrothermal carbonates from the French Massif Central (Allier Valley). Geochim. Cosmochim. Acta. 64, 18, 3189-3199.

Rogers, J. J. W., Satterfield, M.E., 1994. Fluids of Anorogenic Granites: A Preliminary Assessment. Miner. Petrol. 50, 157-171.

Sano, Y., Wakita, H., 1988. Precise measurement of helium isotopes in terrestrial gases. B. Chem. Soc. Jpn. 61, 1153–1157.

Sano, Y., Marty, B., 1995. Origin of carbon in fumarolic gas from island arc. Chem. Geol. 119, 265–74.

Sano Y and Fischer T.P. (2012) The Analysis and Interpretation of Noble Gases in Modern Hydrothermal Systems. In: The noble gases as geochemical tracers, 249-318, Burnard, P. (Ed.)

Sass, J.H., Lachenbruch, A.H., Thermal regime of the Australian continental crust, The Earth: Its Origin, Structure and Evolution, Academic Press, 301-351, 1978.

Saygin E. and Kennett B.L.N., 2010. Ambient noise tomography for the Australian Continent. *Tectonophysics*, 481, 116-125.

Saygin, E., and Kennett B.L.N., 2012. Crustal structure of Australia from ambient seismic noise tomography. *J. Geophys. Res*., 117, B01304; doi:10.1029/2011JB008403.

Saygin, E., McQueen, H., Hutton, L., Kennett, B.L.N., Lister, G., 2013. Structure of Mt Isa and Surroundings from Seismic Ambient Noise Tomography. Aust. J. Earth Sci. 60, 707-718.

Schoell, M., 1980. The hydrogen and carbon isotopic composition of methane from natural gases of various origins. Geochim. Cosmochim. Acta 44, 649-661.

Schoell M. 1988. Multiple origins of methane in the earth. Chem. Geol. 71, 1–10.

Smith, J.W., Pallasser, R. J., 1996. Microbiological origin of Australian coalbed methane. AAPG Bull. 80, 891–97.

Sun, X., 1997. Structural style of the Warburton Basin and control in the Cooper and Eromanga Basins, South Australia. Explor. Geophys. 28, 333–9.

Torgersen, T., Clarke, W.B., 1985. Helium accumulation in groundwater, I: An evaluation of sources and the continental flux of crustal ^{4}He in the Great Artesian Basin, Australia. Geochim. Cosmochim. Acta 49, 1211-1218.

Torgersen, T., Habermehl, M. A., Clarke, W. B., 1992. Crustal helium fluxes and heat flow in the Great Artesian Basin, Australia. Chem. Geol. 102, 139-152.

Trull T.W. and Kurz M.D. (1999) Isotopic fractionation accompanying helium diffusion in basaltic glass. Jour. Molecular Structure, 485/486, 555–567

Uysal, I.T., Feng, Y., Zhao, J.X., Altunel, E., Weatherley, D., Karabacak, V., Cengiz, O., Golding, S.D., Lawrence, M.G. and Collerson, K.D., 2007. U-series dating and geochemical tracing of late Quaternary travertine in co-seismic fissures. Earth Planet. Sc. Lett. 257, 3-4. 450-462.

Uysal, I.T., Feng, Y., Zhao, J.X., Isik, V., Nuriel, P. and Golding, S.D., 2009. Hydrothermal CO_2 degassing in seismically active zones during the late Quaternary. Chem. Geol. 265, 442-454.

Uysal, I.T., Middleton, A.W., and Ring, U., 2013. Understanding the active tectonics in Australia: Implications of geothermal resources. Proceedings Australian Geothermal Energy Conferences 2013 Brisbane, Australia, 14-15 November 2013, p. 99-101.

Vasconcelos, P.M., Knesel K. M., Cohen, B. E., and Heim, J.A. 2008. Geochronology of the Australian Cenozoic: a history of tectonic and igneous activity, weathering, erosion, and sedimentation, Australian Journal of Earth Sciences, 55, 865–914.

Zhang J., Quay P.D., Wilbur D.O. (1995) Carbon isotope fractionation during gas-water exchange and dissolution of CO_2. Geoch. et Cosm. Acta, 59, 1, 107–114

Figure and table captions

Table 1 – Field data, location and basin indication of the investigated bores. Basins labels: M = Millungera; G = Galilee; C = Cooper. Samples from Innot hot springs are not attributed to any basin. Depth is the depth of the base of the screened well section (based on the available information). Coordinates according to the WGS84 Datum. EC= electrical conductivity in μS/cm. ORP = oxidation reduction potential in mV

Table 2 – Chemical composition of the dissolved gases. Data in cc_{gas}/L_{H2O}. Columns 1-7 list the chemical composition calculated by the gas-chromatographic analyses (see text). Concentrations of reactive gases CH_4, CO and H_2 are normally negligible in non-industrial areas as expected for the Australian Outback. ASW = composition of Air Saturated Water reported for comparison

Table 3 – Helium to neon ratios and isotopic composition of helium and carbon. Helium isotopic compositions are reported as R/Ra values together with the measurements errors. Ra_c stands for recalculated values after removal of atmospheric contribution following the procedure described in Hilton (1993). Only samples with $^4He/^{20}Ne>5$ were recalculated. $^4He/^{20}Ne = 0.267$ was used as ASW reference (Holocher et al., 2002). Carbon isotopic composition is reported in δ‰ against V-PDB international standard. The $\delta^{13}C_{CO2}$ values are recalculated from the $\delta^{13}C_{TDC}$ following Zhang et al. (1995). Typical values from natural sources are listed for comparison.

Table 4 – Ar analyses and He concentrations expressed as 10^{-4}vol%. $^{40}Ar^*$ = Argon excess to the atmospheric in ppm by vol.; n.a. = not analyzed;. n.d. = not determined. AIR: atmospheric values reported for comparison.

Table A1 – Comparison of the Birdsville artesian bore data after Torgersen (1992) and our study (this work). We noted a lower temperature (by 10°C) and He/Ne ratio compared to Torgersen et al. (1992) but a higher helium concentration.

Figure 1. – Sample locations over the investigated Millungera, Galilee and Cooper Basins. The sampling sites are spread over an area marked by significant heat-flow anomalies (after OzTemp-Interpreted Temperature at 5km depth, Commonwealth of Australia – Geoscience Australia, 2010) Sample ID shown as open circles in various colours compatible with water temperatures at the well head (see legend)

Figure 2 - Composition of the gases dissolved in the studied waters. The arrows show the trends produced by the addition and dissolution of CO_2 to an atmospheric gas assemblage (see text for details). The grey bar shows the range for mantle volatiles. ASW – Air Saturated Water. Sample symbols: blue diamonds=Millungera Basin; black diamonds=Galilee Basin; red diamonds=Cooper Basin; open black circles=Innot Hot Springs. Samples ID as reported in Tables 1-4

Figure 3a, b. CO_2 content vs (*a*) isotopic composition of $\delta^{13}C_{(CO2)}$ and (*b*) CH_4 concentration. The Cooper Basin broadly shows less negative $\delta^{13}C$ values than the Millungera and Galilee Basins falling close to the typical values of magmatic and hydrothermal CO_2. The evident $\delta^{13}C$-CO_2 relationships account for gas-water interactions (GWI) inducing CO_2 loss and carbon fractionation. The occurrence of similar trends followed by samples from different basins suggests that the content of dissolved CO_2 is not solely controlled by interactions with groundwater, and that the coexistence of multiple sources has to be considered. Figure (b) shows the existence of linear relationships between CO_2 and CH_4. Sample symbols: blue diamonds=Millungera Basin; black diamonds=Galilee Basin; red diamonds=Cooper Basin; open black circles=Innot Hot Springs. Samples ID as reported in Tables 1-4

Figure 4 – CO_2-^3He relationships. $CO_2/^3He$ vs CO_2 content (mlSTP/L_{H2O}) (*a*) and (*b*) $CO_2/^3He$ vs $^3He/^4He$ (R/Ra_c) ratios. Sample symbols: blue diamonds=Millungera Basin; black diamonds=Galilee Basin; red diamonds=Cooper Basin; open black circles=Innot Hot Springs.

Samples ID as reported in Tables 1-4. The shaded area highlights the range of pure MORB-type volatiles. The sample distribution on (*a*) shows trends of CO_2 dissolution at variable extents (dashed lines) with almost constant ^{3}He contents. Figure (b) combines (a) with the information that helium isotopes do not denote simple crust/mantle mixings (see text), however variable $CO_2/^3$He ratios at constant ^{3}He/^{4}He ratios are possible results of subsequent elemental fractionation. All error bars are within the symbols size. Mixing curves in (b) are shown for mantle end-members with 6.5Ra (SCEM, solid lines) and 3Ra (dashed, Mt. Gambier type volatiles; grey areas on top of the plots) with $CO_2/^3$He in the range of $2x10^9$ and $3x10^9$, and crustal end-members with 0.01Ra (radiogenic) and 0.05 (crustal, dotted horizontal lines), and $CO_2/^3$He ratios ranging between 10^9 and 10^{12}.
R/Ra_c = R/Ra corrected for ASW helium = $[R/Ra*(X-1)]/(X-1)$ where X is the ASW-normalized ^{4}He/^{20}Ne ratio taken as 0.267 (Holocher et al., 2002).

Figure 5 - He/Ne vs uncorrected R/Ra relationships of samples from this study and selected samples after Torgersen et al. (1992). The black lines represent mixings of atmospheric and crustal-type (Lower Crust - LC and Upper Crust - UC) helium. Red lines represent 25 (*a*) and 50% (*b*) admixture of subcontinental-type helium (3Ra as from Mt Gambier) to a crustal+atmosphere mixture. Assumed end-members used for the mixing lines: ASW (1 Ra, He/Ne=0.285: Mamyrin and Tolstikhyin, 2004); SCM (3Ra and He/Ne ratio = 1000; e.g Mt.Gambier, Love et al., 2009); Upper Crust and Lower Crust are assumed to have R/Ra=0.02 and He/Ne = 5000, and R/Ra = 0.01 and He/Ne = 5000, respectively. Error bars are smaller than the plotted symbols. Sample symbols: black filled circles=Torgersen et al., 1992; blue diamonds=Millungera Basin; black diamonds=Galilee Basin; red diamonds=Cooper Basin; open black circles=Innot Hot Springs. Samples ID as reported in Tables 1-4

Figure 6 - ^{3}He-^{4}He-CO_2 ternary diagram. The samples are plotted with respect to relative contributions of both helium isotopes after the removal of air contamination. The dotted lines

display the mixing lines between a CO_2 gas phase and helium of different origin (MORB, SCM, AIR, Crust). The effects of progressive CO_2 dissolution as well as the effects of ^3He and ^4He addition are shown by the arrows.

Figure 7 – (*a*) $^{40}Ar/^{36}Ar$ versus $^3He/^4He$ isotopic ratios, and (*b*) $^4He/^{40}Ar$ versus $^3He/^4He$ isotopic ratios. The arrows in figures (*a*) and (*b*) show the concomitant effects on helium and argon isotopes on the addition of crustal and mantle-type volatiles (^{40}Ar increase and R/Ra_c decrease) and argon loss during GWI due to very high Ar solubility. Air values are shown for reference. All values are corrected for atmospheric contamination. Sample symbols: blue diamonds=Millungera Basin; black diamonds=Galilee Basin; red diamonds=Cooper Basin; open black circles=Innot Hot Springs. Samples ID as reported in Tables 1-4

Figure A1 – Theoretical curves of helium permeability rates (PR) through pyrex glass as a function of the inside/outside pressure gradient (ΔP). The curves show the PR through surface areas ranging from 5 to 300 cm^2 (as marked on the curves) for thicknesses of 1 and 3 mm (dashed and thick lines, respectively). Pyrex glass diffusion coefficient of $1.5x10^{-11}$ ccSTPsec/cm^2/mm/Torr (at 25°C) after Norton (1953); pressure gradients calculated for a constant external helium pressure of $5.24x10^{-4}$ KPa ($3.93x10^{-3}$Torr) and variable inside pressures corresponding to helium contents in the range of $1x10^{-4}$ –10 KPa ($4.5x10^{-3}$ - 7.5Torr)

Figure A2 – Full equilibration time between internal and external helium partial pressure (namely sample-atmosphere) as a function of the initial helium content in the range $1\text{-}10^4$ ppm (10^{-2}-1%) for gas bubble volumes of 3, 10 and 240 (gas-filled bottle) ml. The relatively fast helium permeation through pyrex glass does not allow long-term gas sample storage. Water samples for dissolved gas analysis can be stored for a longer time due to the small or negligible volumes of free gas (exsolved gas bubbles) in contact with the pyrex glass walls.

Figure A3 a, b – *a)* Percentage of helium loss as a function of time on a time scale of 10 years as a function of the initial helium content. Three examples are shown for gas bubbles of 5 and 10 cm^3 (dashed and solid lines, respectively) with initial helium contents of 0.005, 0.05 and 0.5% by volume. *b)* Detail of Figure A3a with a time scale of 1 year, showing that storage times shorter than 12 months do not impact on the integrity of the sample for helium concentrations as high as 0.05%. Higher helium contents require a shorter storage time (e.g., for 0.5% [He] and a gas bubble of 5 cm^3 in a 240 ml pyrex glass bottle, a storage time of 3 months would result in a helium loss as high as 2%).

Figure A4 - The plot shows the temporal changes in helium isotopic ratio as a function of the initial helium concentration (here assumed to be 0.5 and 0.05% by volume), the volume of the bubble (10 and 3 cc) and the thickness (0.7 and 3 mm) of the pyrex wall, over a time span of two years. All trends are simulated for an initial isotopic ratio of 0.06 Ra. The red line refers to the sample from the Birdsville well. All simulations show that it is possible to preserve the helium isotopic ratio of the samples over a relatively long time span, as the changes in R/Ra values are smaller than the analytical error (±2%). In our case, changes in the isotopic composition lag behind changes in the concentration (see figures 3a, b)

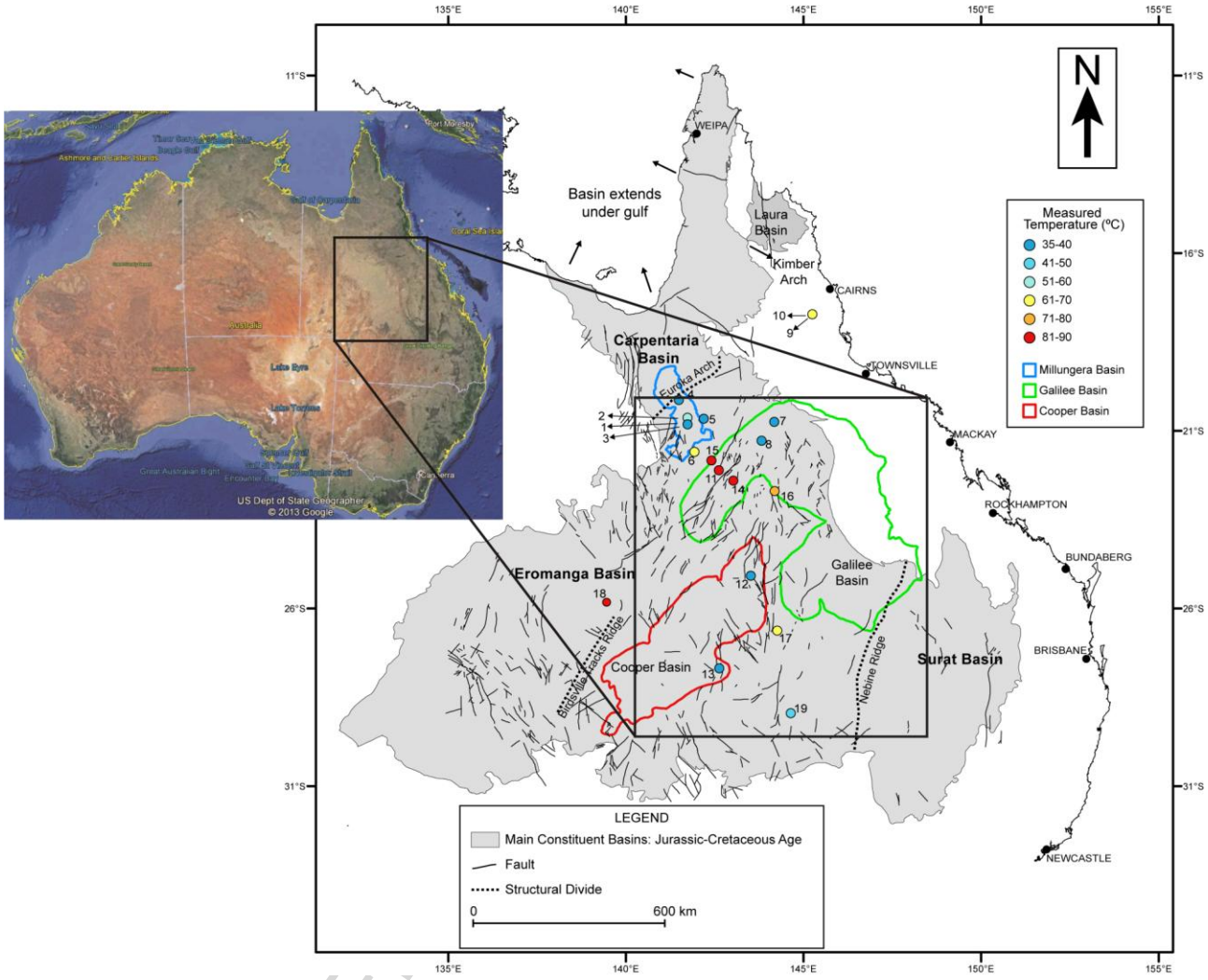

Figure 1

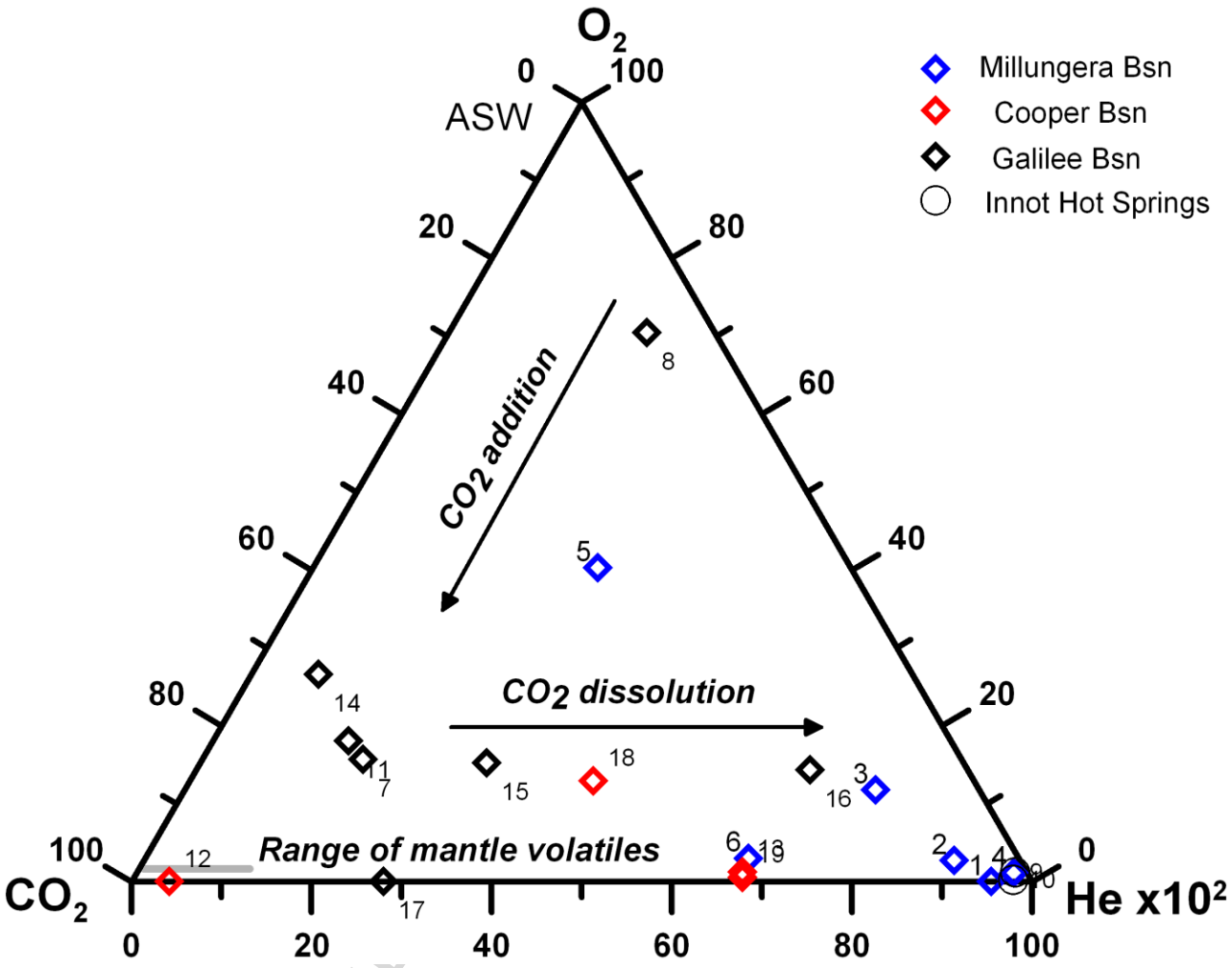

Figure 2

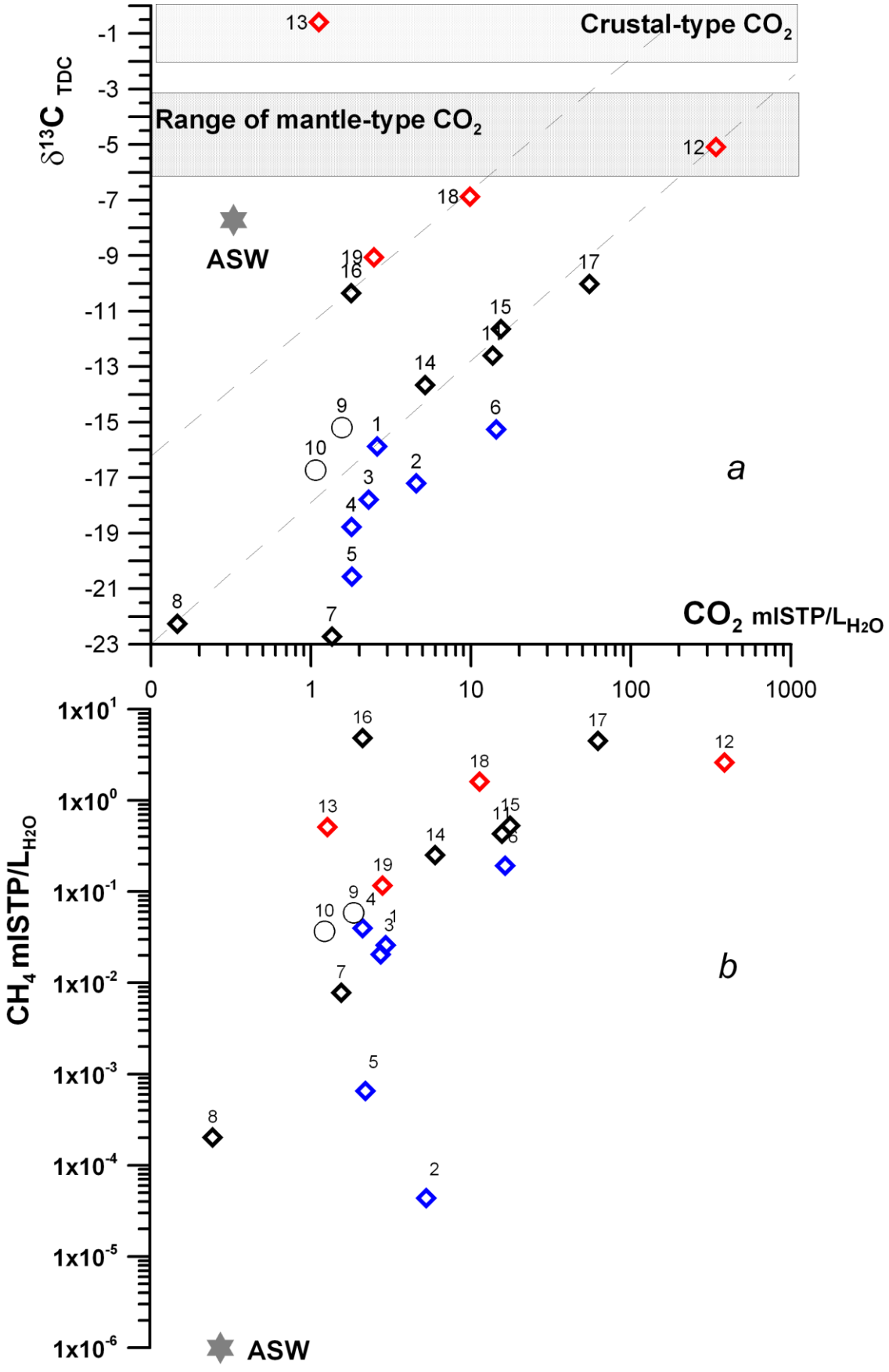

Figure 3

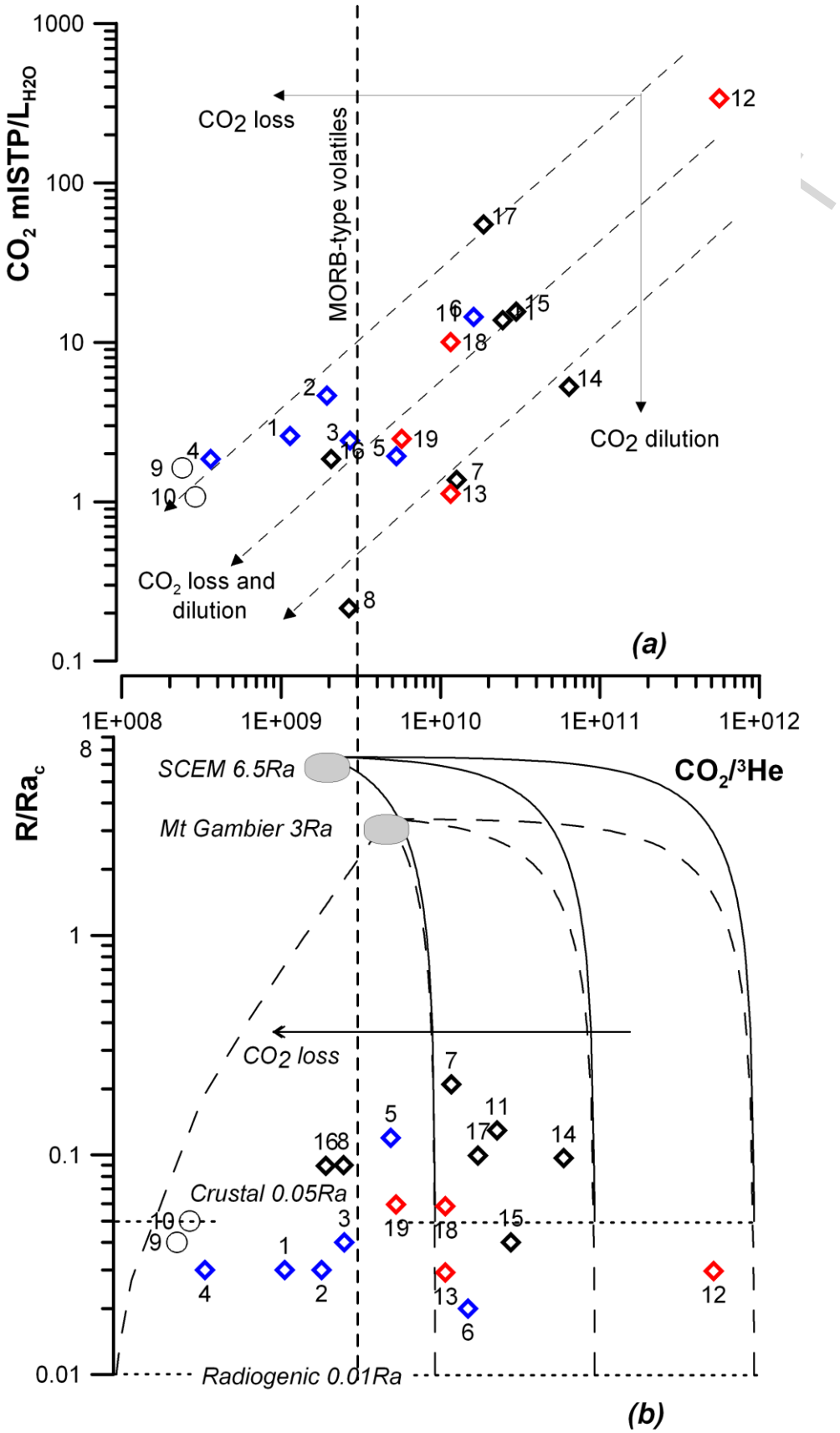

Figure 4

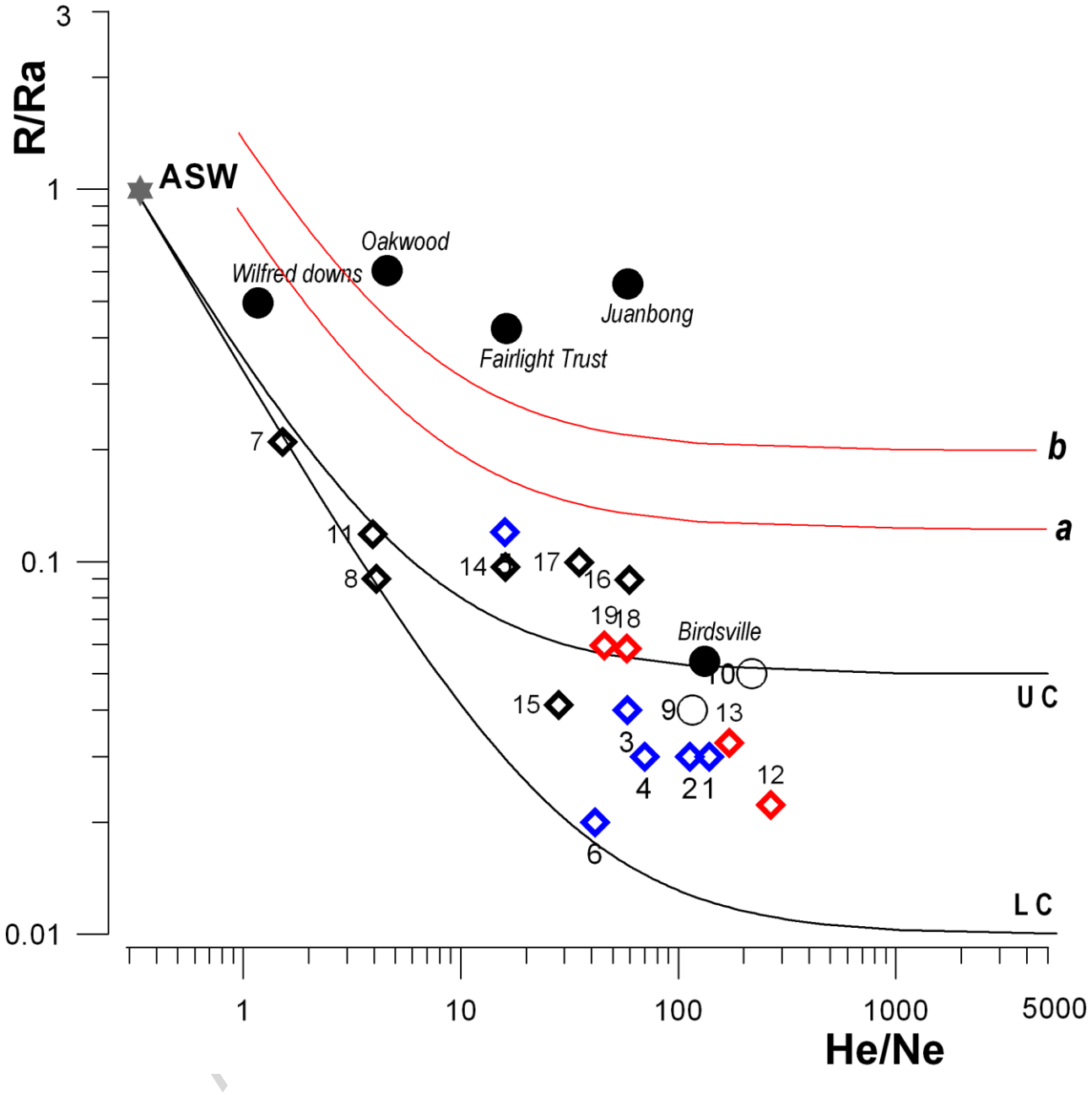

Figure 5

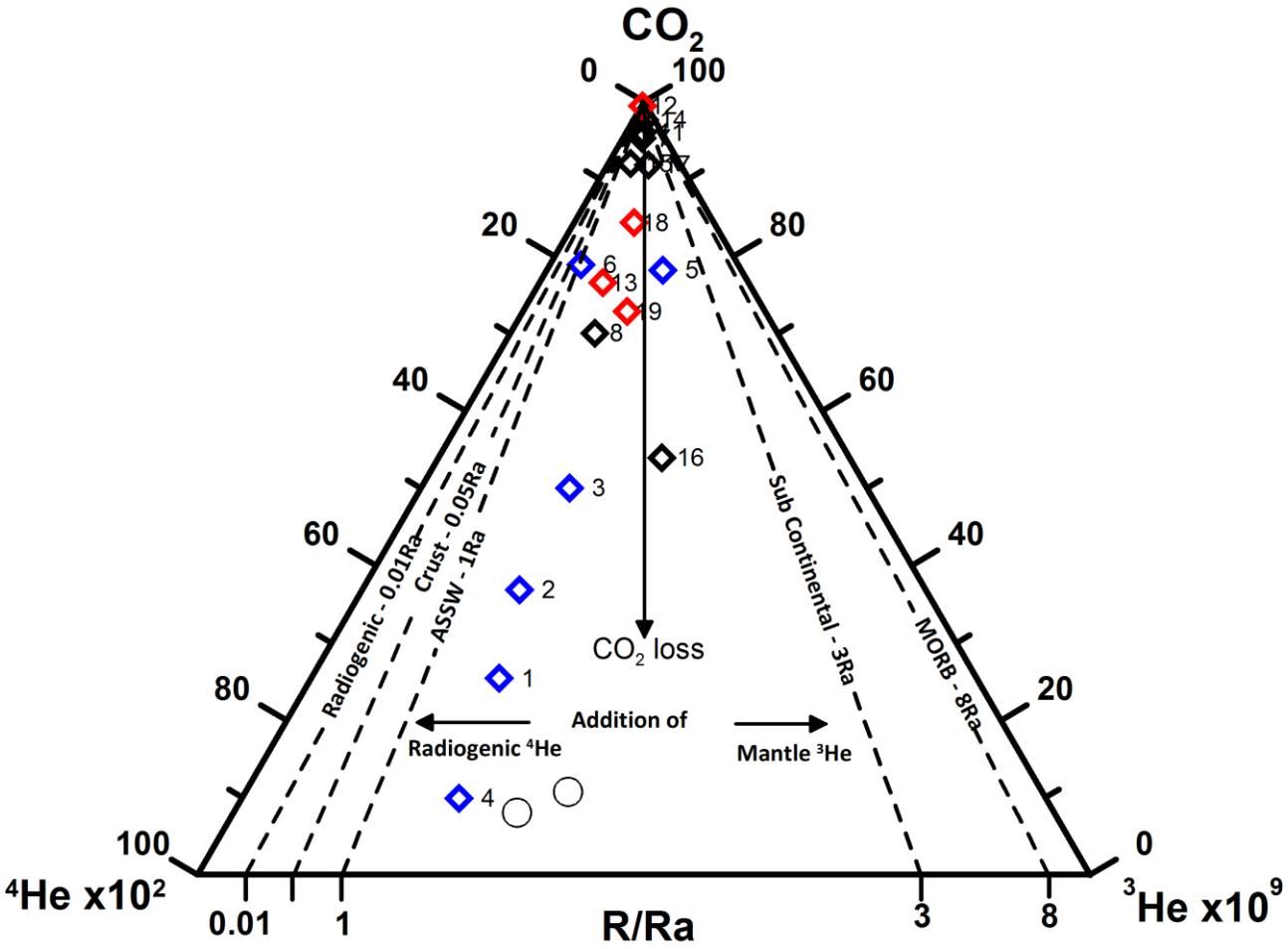

Figure 6

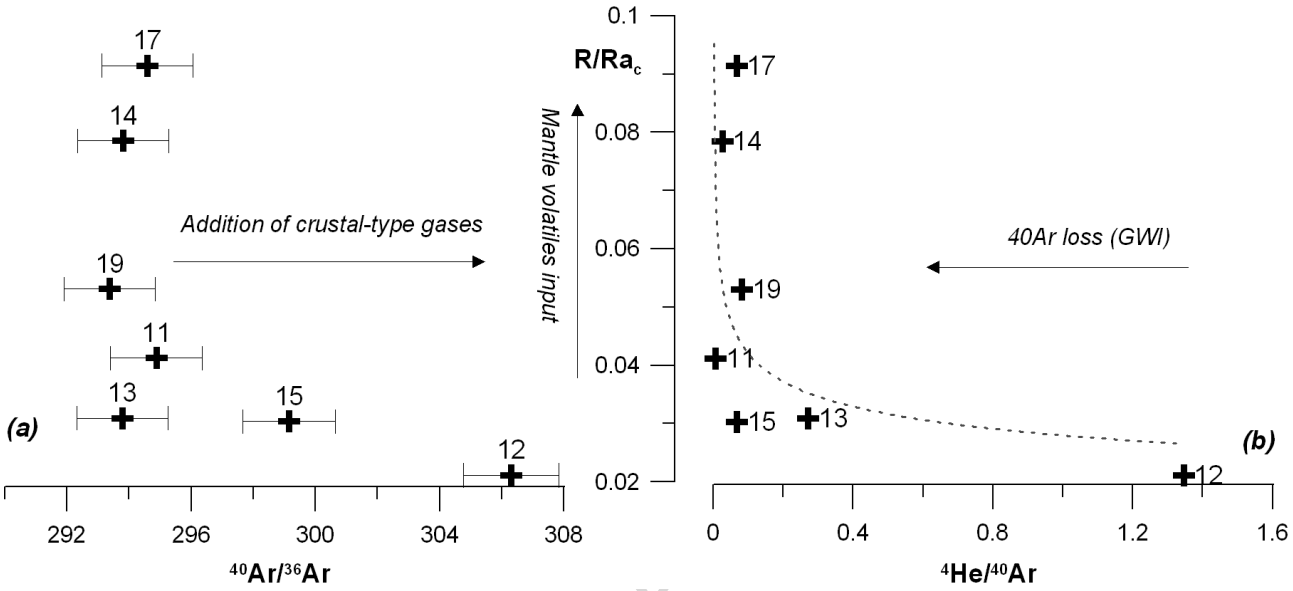

Figure 7

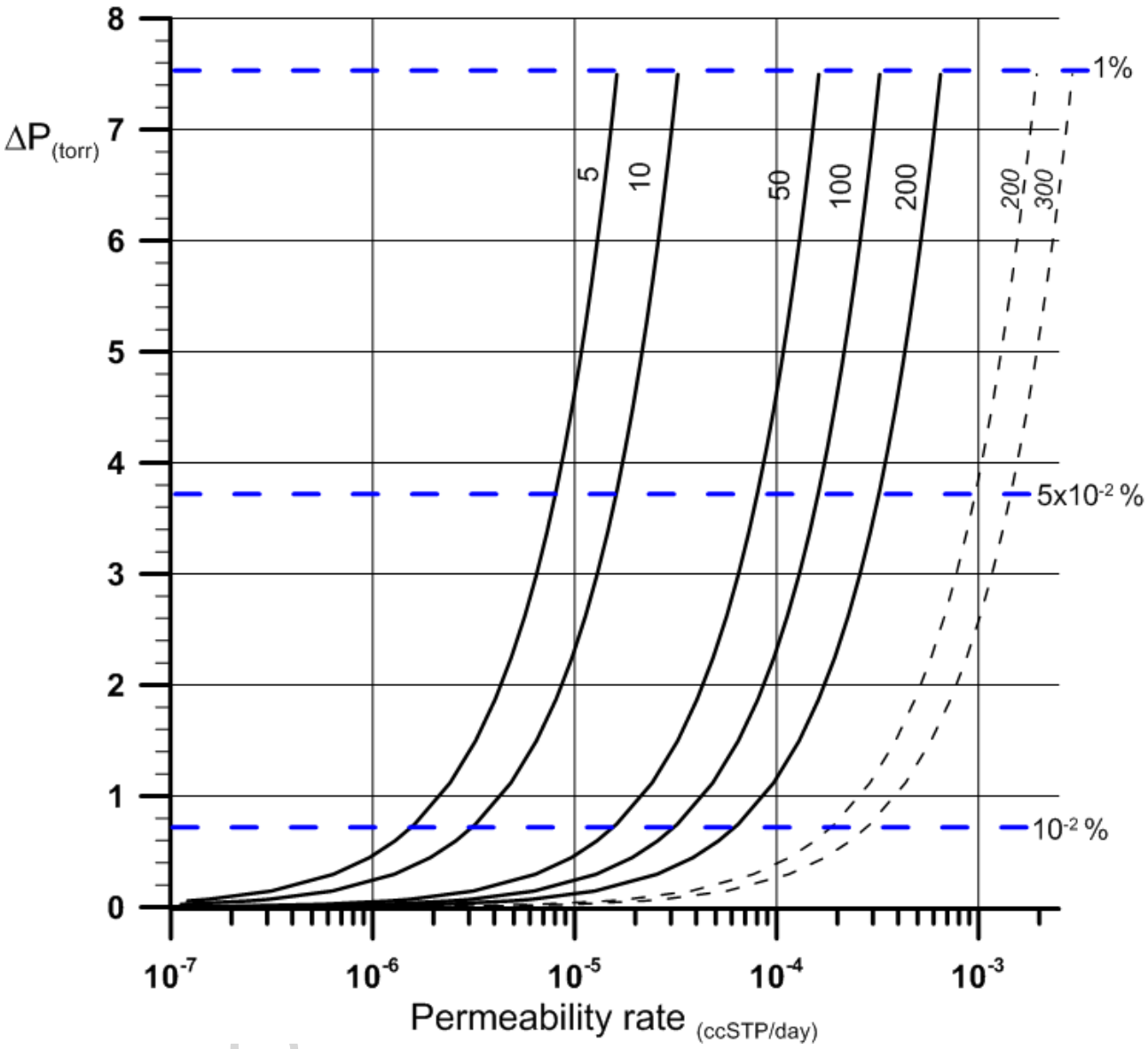

Figure A1

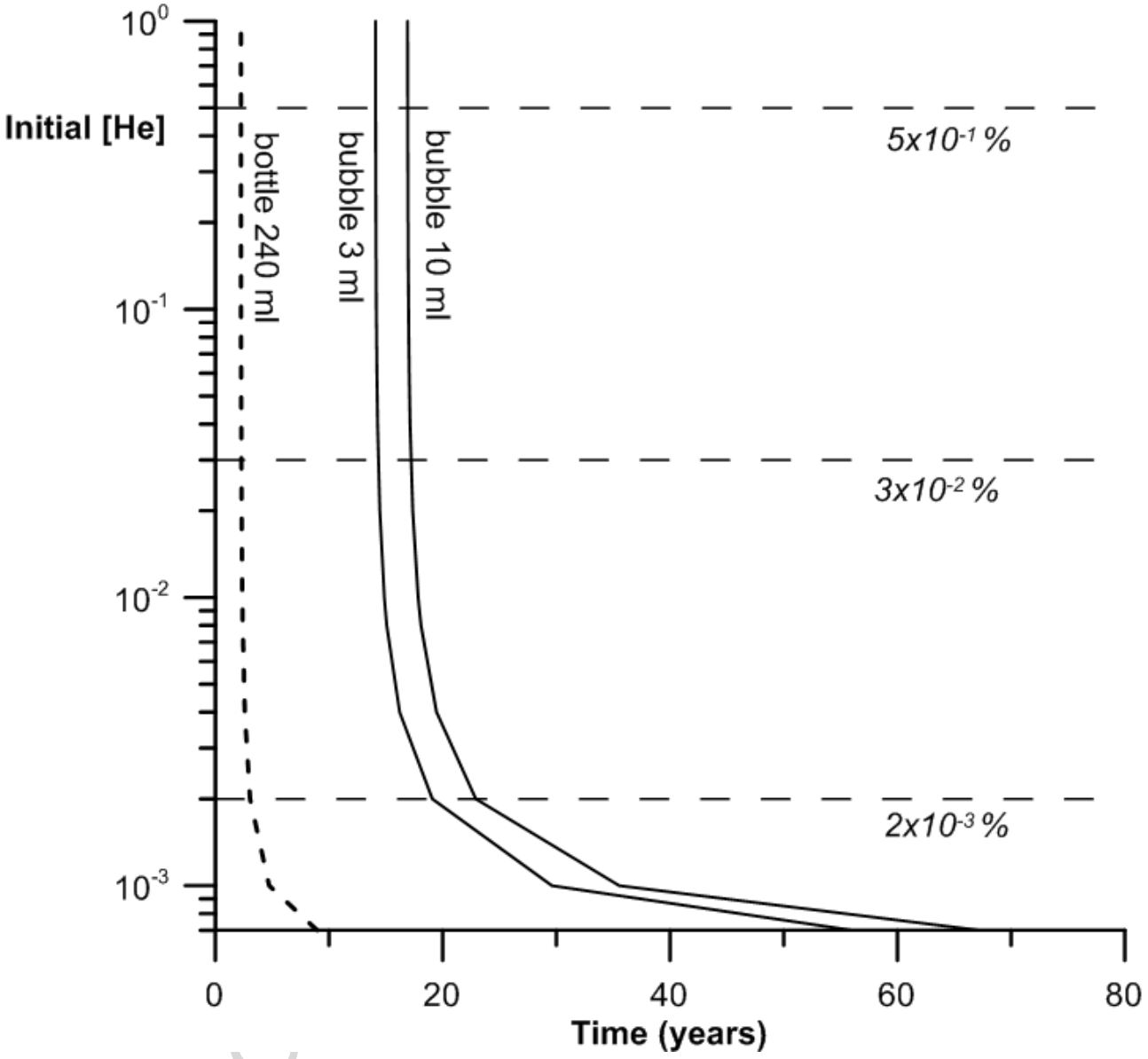

Figure A2

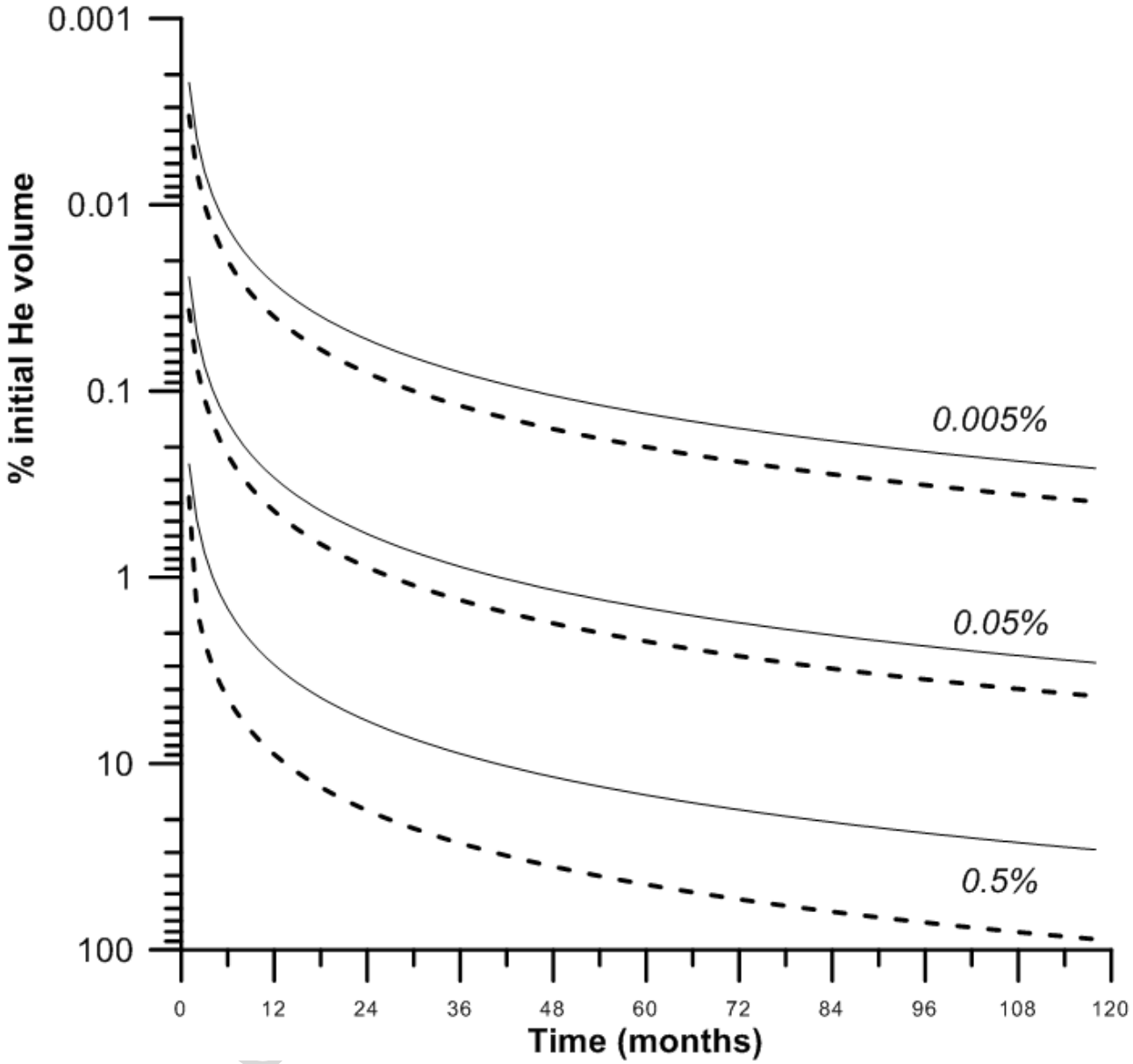

Figure A3a

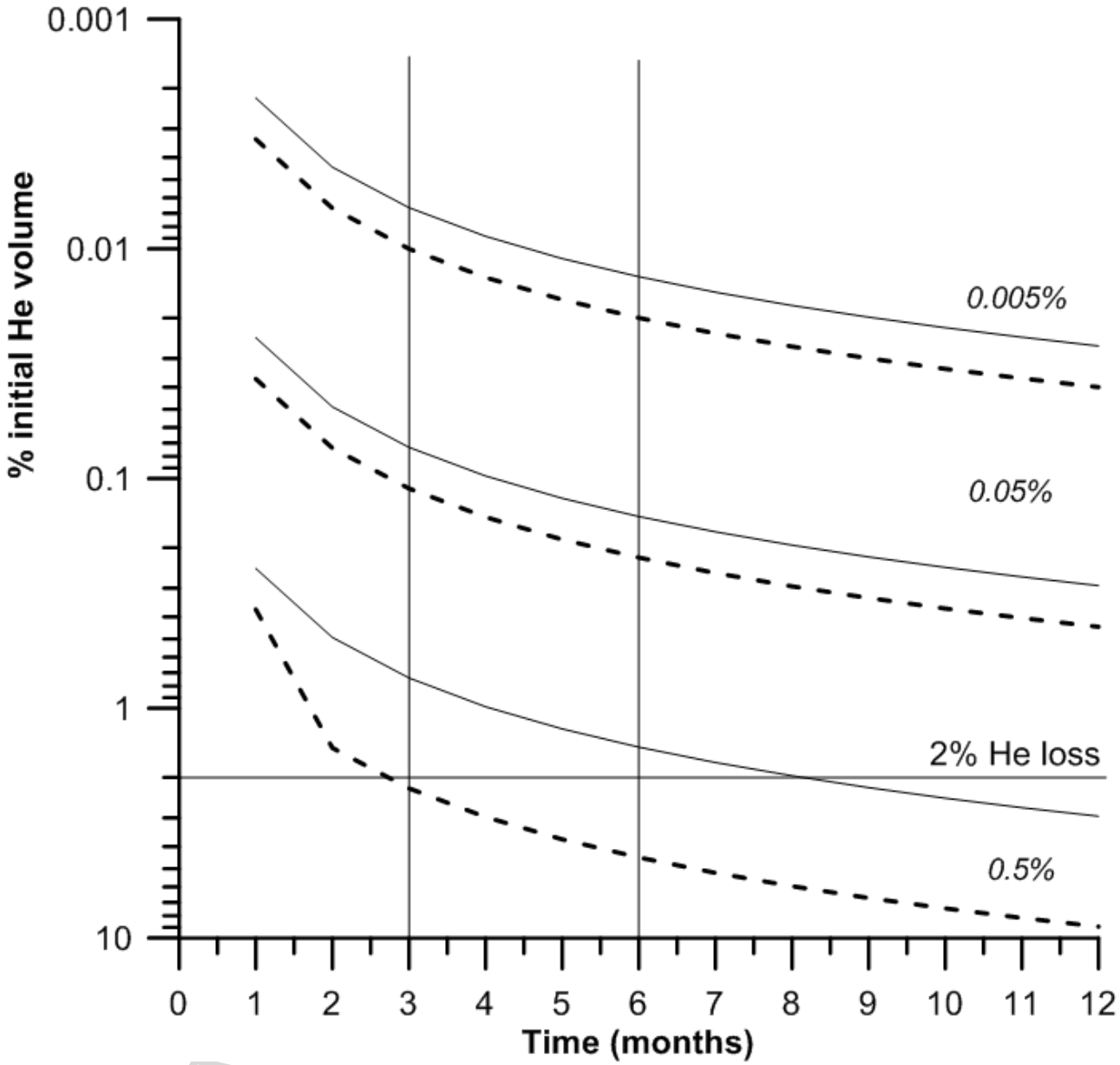

FIGURE A3b

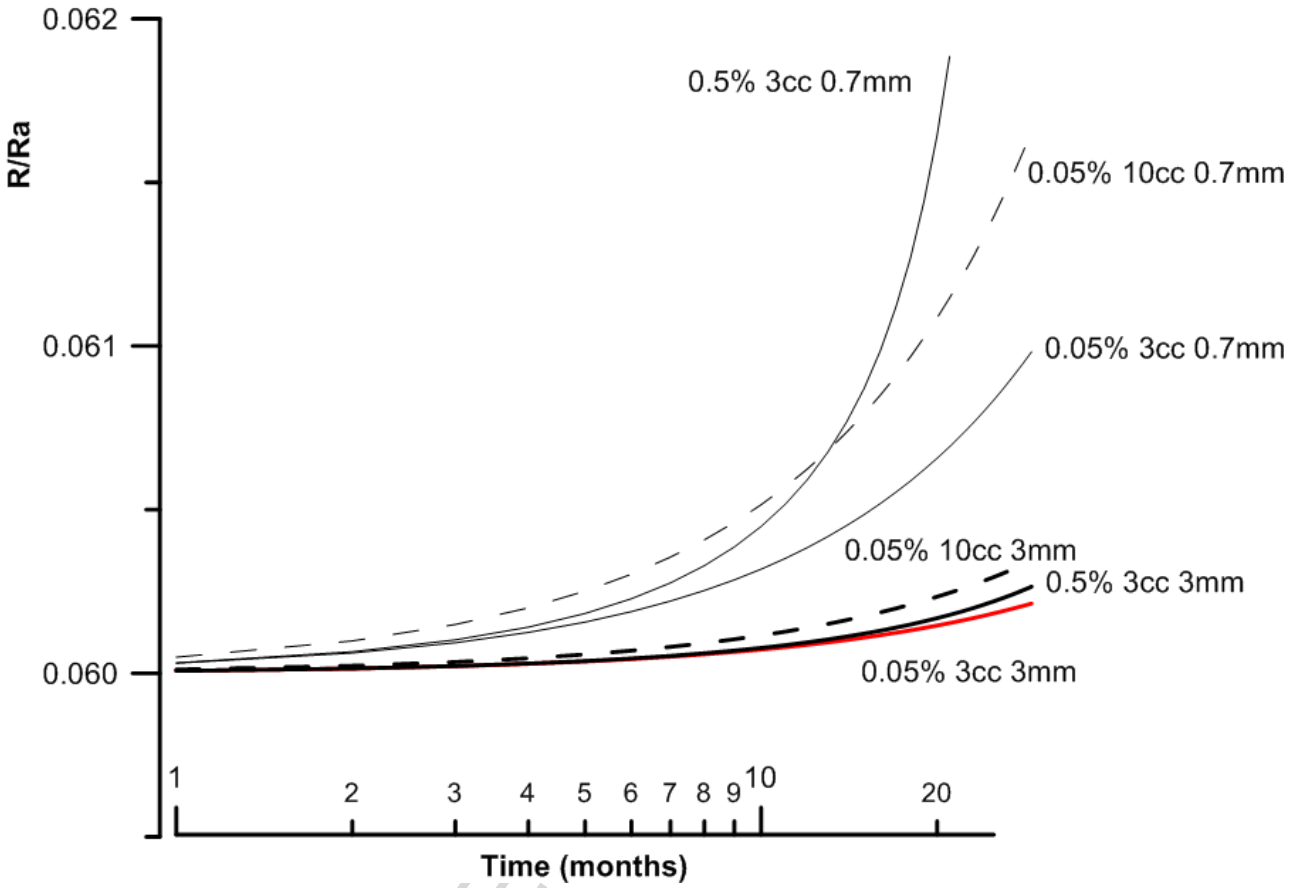

Figure A4

Table 1

Basi	Sample	Sampling site	Date	Depth	Longitud	Latitude	pH	T	EC	ORP
M	1	Julia Creek/Longford	13/12/20	361	20°	141°	7.5	47.0	612	-128
M	2	Julia Creek/Railway	13/12/20	360	20°	141°	7.6	49.1	640	-170
M	3	Julia Creek/Scare-	14/12/20	344	20°	141°	8.0	56.0	641	-60
M	4	Julia Creek/Cabanda	14/12/20	339	20°	141°	8.0	45.1	614	-162
M	5	Julia Creek/Nelie	14/12/20	396	20°	142°	7.9	46.0	493	-57
M	6	Kynuna bore	14/12/20	677	21°	141°	7.5	62.5	645	-200
G	7	Hughenden Shire-	15/12/20	183	20°	144°	8.3	34.5	906	-90
G	8	Hughenden/Stamford	15/12/20	565	21°	143°	8.7	43.0	455	-76
G	11	Weston	10/11/20	1213	22°	142°	7.3	84.0	760	-30
G	14	Winton Town Bore	11/11/20	1222	22°	143°	7.9	86.0	812	-27
G	15	Nuken/Winton	10/11/20	1162	21°	142°	6.8	85.0	817	101
G	16	Greenhills/Longreach	09/11/20	1000	22°	144°	8.1	75.0	840	-32
G	17	Quilpie Town Bore	04/11/20	1200	26°	144°	8.1	61.0	1400	-101
C	12	Bonnie Doon/Jundah	06/11/20	3903	25°	143°	6.1	41.8	6390	-111
C	13	Nockatunga/Noccund	04/11/20	1514	27°	142°	7.1	50.0	2244	-70
C	18	Birdsville	08/11/20	1221	25°	139°	7.7	87.0	1200	-2
C	19	Yowah	05/11/20	691	27°	144°	7.9	57.0	992	-57
	9	Innot Hot Spring/bore	16/12/20	15	17°	145°	7.2	66.2	1041	235
	10	Innot Hot Spring	16/12/20	spring	17°	145°	7.9	68.6	1052	235

Table 2

			1	2	3	4	5	6	7	8
Sample ID	**Site name**	**Basin**	**N_2**	**O_2**	**CO_2**	**CH_4**	**CO**	**H_2**	**He**	**N_2/O_2**
1	Longford Plains	M	10.5	0.02	2.6	2.6E-02	1.70E-05	bdl	5.5E-02	559.9
2	Julia Creek/Railway	M	4.6	1.70	4.6	4.4E-05	1.84E-05	bdl	5.6E-02	2.7
3	Julia Creek/Scare-bore	M	10.2	2.35	2.4	2.1E-02	7.93E-04	3.9E-04	1.5E-02	4.4
4	Cabanda	M	16.5	1.36	1.9	4.0E-02	2.99E-05	6.1E-03	1.2E-01	12.2
5	Nelie	M	8.8	2.58	1.9	6.5E-04	2.80E-05	bdl	2.0E-03	3.4
6	Kynuna	M	16.7	1.44	14.4	1.9E-01	5.12E-04	2.8E-03	3.2E-02	11.6
7	Hughenden Shire-bore	G	17.7	0.32	1.4	7.8E-03	5.45E-04	bdl	3.7E-04	55.4
8	Hughenden Stamford	G	11.1	1.37	0.2	2.0E-04	1.34E-05	bdl	4.4E-04	8.1
11	Weston	G	15.9	3.69	13.8	4.3E-01	9.7E-04	2.2E-02	3.1E-03	4.3
14	Winton	G	7.8	2.09	5.3	2.5E-01	6.9E-04	2.5E-03	6.0E-04	3.7
15	Nuken	G	26.0	4.42	15.6	5.3E-01	2.4E-04	5.5E-04	9.2E-03	5.9
16	Longreach	G	7.0	1.46	1.9	4.9E+00	5.2E-06	6.3E-04	7.0E-03	4.8
17	Quilpie	G	5.0	0.04	54.9	4.5E+00	9.3E-04	3.2E-02	2.1E-02	119.1
12	Bonnie Doon	C	2.1	0.05	339.7	2.6E+00	2.9E-05	bdl	1.5E-02	43.6
13	Nockatunga	C	8.3	0.05	1.1	5.1E-01	1.0E-03	2.6E-01	2.4E-03	182.8
18	Birdsville	C	19.7	3.02	10.0	1.6E+00	1.0E-03	1.4E-02	1.0E-02	6.5
19	Yowah	C	8.6	0.04	2.5	1.2E-01	0.0E+00	4.2E-04	5.2E-03	194.3
9	Innot Hot bore		15.2	1.43	1.6	5.9E-02	1.87E-05	bdl	1.2E-01	10.6
10	Innot Hot Spring		8.2	0.12	1.1	3.7E-02	5.73E-04	1.9E-02	5.3E-02	66.2
	ASW		***9.6***	***4.8***	***0.24***	***<1E-5***	***<1E-6***	***<1E-6***	***4.8E-5***	***2.0***

Table 3

Sample ID	Basin	Site name	R/Ra	He/Ne	R/Rac	$\delta^{13}C_{TDC}$	$\delta^{13}C_{CO2}$
1	M	Longford Plains	0.03±0.003	139.12	0.03	-13.70	-16.05
2	M	Julia Creek/Railway	0.03±0.002	113.23	0.03	-14.62	-17.05
3	M	Julia Creek/Scare-bore	0.04±0.001	58.20	0.04	-14.52	-16.91
4	M	Cabanda	0.03±0.003	69.97	0.03	-14.55	-17.70
5	M	Nelie	0.12±0.003	15.97	0.10	-16.86	-19.79
6	M	Kynuna	0.02±0.001	41.51	0.01	-13.94	-15.39
7	G	Hughenden Shire-bore	0.21±0.013	1.52	--	-16.91	-21.08
8	G	Hughenden Stamford	0.09±0.011	4.09	--	-16.86	-20.70
11	G	Weston	0.12±0.014	3.95	--	-12.63	-12.76
14	G	Winton	0.10±0.026	16.04	0.08	-13.19	-13.43
15	G	Nuken	0.04±0.007	28.24	0.03	-12.19	-11.90
16	G	Longreach	0.09±0.0015	59.67	0.09	-8.70	n.d.
17	G	Quilpie	0.10±0.018	35.07	0.09	-7.18	-9.23
12	C	Bonnie Doon	0.02±0.0012	265.77	0.02	-5.89	-2.36
13	C	Nockatunga	0.03±0.0012	171.44	0.03	0.18	-1.37
18	C	Birdsville	0.06±0.0012	57.82	0.05	-6.69	-6.80
19	C	Yowah	0.06±0.0013	45.59	0.05	-6.11	-8.35
9		Innot Hot bore	0.04±0.004	116.21	0.04	-14.67	-15.64
10		Innot Hot Spring	0.05±0.002	217.90	0.05	-14.67	-16.14
ASW			*1*	*0.267*			*-7**
Volcanic fluids			*2 to 7*	*>1000*			*-7 to 0*
MORB			*8*	*>1000*			*-6.5*
Crustal fluids			*0.05*	*>1000*			*-2 to 2*
Radiogenic fluids			*0.01*	*>1000*			*n.d.*
Biogenic fluids			*n.d.*	*n.d.*			*<-20*

Table 4

Sample ID	Basin	Site name	^{4}He	^{40}Ar	^{38}Ar	^{36}Ar	^{40}Ar*	^{40}Ar/^{36}Arc
11	G	Weston	76.5	12240.7	7.7	41.3	28.8	294.9
14	G	Winton	297.3	11711.6	7.4	39.7	n.d	293.8
15	G	Nuken	559.1	8357.3	5.2	27.8	139.4	299.1
17	G	Quilpie	733.1	11057.3	7.0	37.4	14.0	294.6
12	C	Bonnie Doon	1631.0	1211.6	0.7	3.9	47.7	306.3
13	C	Nockatunga	2079.2	7668.6	4.9	26.0	n.d.	293.8
19	C	Yowah	967.0	11904.3				293.4
		AIR	*5.2*	*9780.0*	*6.2*	*33.1*		*295.5*

Table A1

BIRDSVILLE	Bore N°	Longitude	Latitude	T°C	R/Ra	He/Ne	R/Rac	[He] ccSTP/L
This work	14645	25° 51`44”	139° 28`22”	87	0.06±0.0012	57.8	0.05	$1x10^{-2}$
Torgersen et al (1992)	14645	-25.8966	139.3519	97	0.0696	129	0.05	$4.68x10^{-3}$

Appendix

Helium permeation through pyrex glass

Helium diffusion through pyrex glass is known to be a potentially serious problem for sample storage before helium isotope analysis due to the rate of helium diffusion through pyrex glass bottles (e.g. Sano and Fisher, 2012). For this reason, pyrex bottles are not commonly used for the collection of fluids/gases for helium isotope analysis. However, as As the optimization of sampling and analytical methods must be based on scientific evidence, all the available experimental information must be considered before a certain procedure can be adopted or deemed to be unsuitable for a specific purpose. In this appendix, we review the available evidence for He diffusivity through pyrex glass, and argue that pyrex glass bottles are suitable for the sampling and storage of fluids/gases for He isotope analysis as long as the storage time does not exceed two months.

In a recent paper by Sano and Fisher (2012), the problem of long-time storage of samples for helium isotopic analysis is discussed considering the permeation constants of pyrex glass of 1.5×10^{-11} ccSTP/sec/cm^2/mm/Torr (at 25°C), experimentally determined by Norton (1953). Sano and Fisher (2012) The authors calculated a permeation rate of 3.2×10^{-6} ccSTP/day of total helium for a pyrex bottle of with 280 cm^2 inner surface area, 0.7 mm thick glass, 300 ml of internal volume, with an internal helium concentration of 1.3 vol% and atmospheric helium concentration outside the bottle ($\Delta P \approx 10$Torr = 7.5×10^{-2}Pa). Taking into consideration Under the above-mentionedthese conditions, it would take the sample will take 10 years for the sample to equilibrate with the atmosphere. This is a short time if compared to lead glass, whose permeation constant is lower by one order of magnitude (9.1×10^{-12}; ccSTP/sec/cm^2/mm/Torr; Norton, 1953), and thus implying an equilibration time of the order of one century.

Figure A1 A1 A4 shows the permeability rates as a function of the He partial pressure gradient for different surface areas and thicknesses. Considering a helium concentration inside the pyrex bottle of 100 ppm (10^{-2}%), the permeability rate spans ranges from $1.5x10^{-6}$ to $3x10^{-4}$ ccSTP/day.: The range is $1x10^{-5}$ to $2x10^{-3}$ ccSTP/day for a 1% He concentration, the range is $1x10^{-5}$ to $2x10^{-3}$ ccSTP/day . At this rate, a gas sample stored in our 240 ml pyrex bottles (inner surface area of 367 cm^2) and 3mm wall thickness), will take about 10 years to equilibrate with the atmospheric helium concentration, almost irrespective of the initial He concentration within the range 100 ppm - to 1% (Figure A2).

Since the permeation constantspermeability rates are direct and linear functions of surface area, area?, time and inside/outside concentration gradient, and inverse function of the thickness, a decrease of thein helium concentration lower by an order of magnitude leads to an equilibration time of one millennium for leaded glass. Therefore, a storage time of up to 2-3 years in leaded glass will not compromise the sample's integrity (Sano and Fisher, 2012).

The case of water samples for dissolved gas analyses.

The case of water samples for dissolved gas analyses.

Water Ssamples collected for dissolved gas analyses are typically water samples that require further laboratory procedures for gas extraction. As a consequence, tThe sampling bottles are not filled by with gas, thus and therefore the pyrex glass surface area through which helium can permeate the through the pyrex glass is not the whole inner surface area of the bottle, but only that of the gas bubble created formed because ofby gas exsolution and/or because of water volume contraction due to cooling. For example, for a 240 ml water sample collected at 85 °C, a temperature drop of from 60 °C to room temperature (assumed to be 25 °C) generates a volume contraction of 93.0.24 ml (estimated considering the volumetric expansion relationship for liquids $\Delta V=3KV_0\Delta T$, where K=volumetric thermal expansion coefficient for water = $2.14x10^{-4}$ $°C^{-1}$ and for V_0=240 ml), which

creates a bubble that is filled by with gases exsolved from the water. From that time on, hHelium can permeate diffuse from this bubble through the glass, but and since the diffusion is a matter ofpermeability rate is a function of surface area and thickness of the wall, as well as of the inside/outside helium concentration gradient. Under these conditions, , the equilibration time between the sample helium and atmospheric helium takes to equilibrate with the atmosphere becomes much longer because of the small exchange surface, although it might also be shorter due to the small low amount of helium contained in the gas bubble.

Figure A2 shows three time-dependent trends for the full equilibration of sample helium (inside) with the atmosphere (outside), calculated for gas sampler volumes of 3, 10 and 240 ml (representative for bubbles generated by temperature drops of 25 and 60 °C and for a gas-filled bottle, respectively). The horizontal lines highlight the initial sample helium contents of 0.5, 0.03 and 0.002% (ranges recorded in our sample sets suite). The relatively wide concentration range we considered in these calculations also takes also into account the helium enrichment in the separated gas phase due to its low solubility in the water phase. It is easy straightforward to observe that gas in the a completely-filled bottle completely filled with gas takes a relatively short time to equilibrate with the atmosphere (about 10 years for the considered range of helium contents). In contrast, the gas bubbles need 5 times (or even) longer (or even more) to equilibrate with the atmosphere due to their reduced exchange surface areas (we even considered considering the maximum spherical section). The conclusion of our calculations is that a long-term storage cannot be considered a reliable procedure for gas samples collected in pyrex bottles, ; however, it is suitable for water samples as long as the storage time does not exceed a few months.

Samples collected in pyrex bottles during the course offor this work arestudy were analyzed typically within two-three to four weeks. Our samples were collected in two runs and all analyzed within three weeks from the date of sampling. The first batch was sampled between 5 to 11 November 2011, and the second from 13 to 16 December 2011. All samples were shipped to Italy

by fast cargo and were analyzed on 25 November 2011 (first batch) and 9-10 January 2012 (second batch). The maximum He loss within this time frame (from three weeks to one month) would be 0.3% (for a biglarge-size bubble with the highest helium content of 0.5% by volume) of the initial content (Figure A3 a, b). For these reasons, we consider the $^{3}He/^{4}He$ values reported in Table 3 as representative of the aquifers waters sampled.

We also note that hHelium isotopes can also be fractionated during helium permeation because of the different diffusivity of masses 3 and 4. Following Trull and Kurtz (1999), low isotopic diffusivity ratios ($D^{3}He/D^{4}He$) require significantly large He losses to alter the initial $^{3}He/^{4}He$ ratios. Considering a $D^{3}He/D^{4}He=1.15$ (at room temperature - from Graham's Law), the initial $^{3}He/^{4}He$ ratio may be lowered by 10% for a 65% He loss. This value increases to 80% for a diffusivity ratio of 1.08 (Trull and Kurtz, 1999). Considering that the helium loss from our samples is always below 0.5% (even in the worst-case scenario of 0.5% initial He content – see Figure A3b), the resulting isotopic fractionation is negligible and within the measurements error.

Further simulation tests have been done carried out to evaluate the temporal changes in the isotopic ratio due to the contemporary simultaneous ^{4}He-outletloss/ ^{3}He-inlet gain through the pyrex walls induced by the different pressure gradients of the two massesisotopes. Figure A4 shows the simulations built for 0.7 and 3 mm pyrex glass wall thicknesses with internal helium contents of 0.5 and 0.05%. The ^{3}He inner partial pressure for in the dissolved gas sample es is calculated by from the helium content, the total gas content and the gas/water partition coefficients as a function of the temperature. For example, the sample "Birdsville" sample ($^{3}He/^{4}He$ ratio = 0.06 Ra) has a helium content of $1x10^{-2}$ ccSTP/L and a total gas amount content of 35,.36 ccSTP/L (Table 2). These values yield giving a ^{3}He partial pressure of $9.86x10^{-8}$ hPa, which is an order of magnitude higher than the atmosphere ($7.28x10^{-9}$hPa). This ^{3}He pressures range, always higher than the atmosphere, avoids prevents atmospheric ^{3}He permeation from the outside, always causing aand isotopic

fractionation as a function of sample storage time temporal decreasing trend for both helium content and isotopic ratio.

As a result of the above calculations and considerations, we recommend that samples collected in pyrex glass bottles for dissolved gas helium analyses must be measured within 3-6 months (depending on their original helium content) from the date of collection.

This kind ofWe further note that pyrex glass bottles are not suitable for the long-term storage of water samples are also unsuitable for longer storage because of potential helium leakage through the rubber septum. To avoid atmospheric helium diffusion through the septum, we kept the bottles upside down and with the necks submerged in salty water even during sample shipping and laboratory handling.

The measured helium isotopic ratios in this work, well below the atmospheric value,s are consistent with a lack of atmospheric contamination due to ^{3}He permeation through the pyrex or the septum as a consequence of the large ^{3}He partial pressure difference between air and our the samples. The results we have obtained in previous studies using the same sampling equipment and methods (e.g., Italiano et al., 2013 and references therein) show that these precautions make our methodology suitable for the analytical determinations on of all dissolved gases (including all the main gases, chemical composition, helium and other noble gases and their isotopic composition, and isotopes total dissolved carbon isotopesand carbon isotopic ratio of TDC).

To conclude, although no duplicate samples were collected using different containers, we note that the helium isotopic ratios measured in a sample from a the Birdsville well at Birdsville (Table A1) collected in copper tubes by Torgersen (1992) and our sample collected twenty years later at from the same well but in using a pyrex bottles are virtually identical.

TABLE AND FIGURES CAPTIONS

Table A1 – Comparison of the Birdsville artesian bore data after Torgersen (1992) and our study (this work). We noted a lower temperature (by 10°C) and He/Ne ratio compared to Torgersen et al. (1992) but a higher helium concentration.

Figure A1 – Theoretical curves forof helium permeability rates (PR) through pyrex glass as a function of the inside/outside pressure gradient (ΔP). The curves show the PR through surface areas in the range ofranging from 5 to -300 cm^2 (see labelsas marked on the curves) for thicknesses of 1 and 3 mm (dashed and thick lines, respectively). Pyrex glass dDiffusion coefficient of $1.5x10^{-11}$ ccSTPsec/cm^2/mm/Torr (at 25°C) after Norton (1953); pressure gradients calculated for a fixedconstant external helium pressure of $5.24x10^{-4}$ KPa ($3.93x10^{-3}$Torr) and variable inside pressures for variablecorresponding to helium contents in the range of $1x10^{-4}$ –10 KPa ($4.5x10^{-3}$ - 7.5Torr)

Figure A2 – Full equilibration time between internal and external helium partial pressure (namely sample-atmosphere) as a function of the initial helium content in the range $1\text{-}10^4$ ppm (10^{-2}-1%) for gas bubble bottle volumes of 3, 10 and 240 (gas-filled bottle) ml. The relatively fast helium permeation through pyrex glass doesn't not allow long-term laboratory gas samples storage. The wWater samples for dissolved gas analysis can be stored for a longer time represent a different case due to the small or negligible volumes of free gas (exsolved gas bubbles) in contact with the pyrex glass walls.

Figure A3 a, b – a) Percentage of helium loss as a function of time on a time scale of 10 years as a function of the initial helium content. Three examples are shown for gas bubbles of 5 and 10 cm^3

(dashed and solid lines, respectively) with initial helium contents of 0.005, 0.05 and 0.5% by volume. b) Ddetails of Figure A3a with a time scale of 1 year, showing that storage times shorter than 12 months does not impact on the integrity of the sample for helium concentrations as high as 0.05%. Higher helium contents require a shorter storage time (e.g., for 0.5% [He] and a gas bubble of 5 cm^3 in a 240 ml pyrex glass bottle, a storage time of 3 months would result in a helium loss as high as 2%).

BIRDSVILLE	Bore N°	Longitude	Latitude	T°C	R/Ra	He/Ne	R/Rac	[He] ccSTP/L
Our sampleTthis	14645	25° 51`44"	139° 28`22"	87	0.06±0.0012	57.8	0.05	$1x10^{-2}$
Torgersen et al (1992)	14645	-25.8966	139.3519	97	0.0696	129	0.05	$4.68x10^{-3}$

Figure A4 - The plot shows the temporal changes in helium isotopic ratio as a function of the initial helium concentration (here assumed to be 0.5 and 0.05% by volume), the volume of the bubble (10 and 3 cc) and the thickness (0.7 and 3 mm) of the pyrex wall, over a time span of two years. All trends are simulated for an initial isotopic ratio of 0.06 Ra. The red line refers to the sample from the Birdsville well. All simulations show that it is possible to preserve the helium isotopic ratio of the samples over a relatively long time span, as the changes in R/Ra values are smaller than the analytical error (±2%). In our case, changes in the isotopic composition lag behind changes in the concentration (see figures 3a, b)

Highlights

Artesian waters of the GAB carry crustal and mantle sourced CO_2-dominated dissolved gases

High crustal-helium partial pressure at depth masks mantle-type He in dissolved gases

Mantle He is present in the west-central part of the GAB despite no evidence of young volcanism

Mantle He degassing may be related to neotectonics in central Australia and deep litospheric faults